Improved cooperative competitive particle swarm optimization and nonlinear coefficient temperature decreasing simulated annealing-back propagation methods for state of health estimation of energy storage batteries.

XIONG, R., WANG, S., HUANG, Q., YU, C., FERNANDEZ, C., XIAO, W., JIA, J. and GUERRERO, J.M.

2024

Improved cooperative competitive particle swarm optimization and nonlinear coefficient temperature decreasing simulated annealing-back propagation methods for state of health estimation of energy storage batteries

Ran Xiong[1,2,3], Shunli Wang[1,2,*], Qi Huang[1], Chunmei Yu[1], Carlos Fernandez[4], Wei Xiao[3], Jun Jia[3], Josep M. Guerrero[5]

[1]School of Information Engineering, Southwest University of Science and Technology, Mianyang, 621010, China;

[2]College of Electrical Engineering, Sichuan University, Chengdu, 610065, China;

[3]Sichuan Energy Internet Research Institute, Tsinghua University, Chengdu, 610042, China;

[4]School of Pharmacy and Life Sciences, Robert Gordon University, Aberdeen, AB10-7GJ, UK;

[5]Department of Energy Technology, Aalborg University, Aalborg, 9200, Denmark.

Abstract: At present, the accurate establishment of the battery model and the effective state of health (SOH) estimation under actual energy storage conditions have become the main problems in new energy storage stations. Therefore, a SOH estimation method based on cooperative competitive particle swarm optimization (CCPSO) and nonlinear coefficient temperature decreasing simulated annealing-back propagation (NSA-BP) is proposed. The novelty of this research mainly includes the design of extraction methods in different health indicators (HIs) and the construction of developed NSA-BP network for SOH estimation. In this research, the contributions of SOH estimation are mainly to assist in battery replacement and provide relevant economic reference. Low-rate constant current energy storage degradation experiments and a variable-rate energy storage degradation experiment are performed for different battery packs at 25 ℃. The experimental results indicate that the root mean square error (RMSE) and the mean absolute error (MAE) of the proposed method are 0.00588 and 0.00481 under the 0.5 rate condition, and the corresponding values are 0.00732 and 0.00639 under the variable-rate condition. Under the same condition, the proposed SOH estimation method is superior to the methods before improvement in RMSE and MAE, which can provide a basis for efficient monitoring of energy storage batteries.

Key words: Energy storage lithium-ion battery; Nonlinear coefficient temperature decreasing simulated annealing; Cooperative competitive particle swarm optimization; State of health; Health indicators

***Corresponding author**: Shunli Wang. Tel: +86-15884655563. E-mail address: 497420789@qq.com.

1. Introduction

Due to the significant changes in the power structure, electrochemical energy storage becomes popular [1, 2]. The safe use of lithium-ion (Li-ion) batteries and the efficient estimation of battery states are necessary [3, 4]. One of main functions of battery management system (BMS) is to ensure the safe and stable operation by efficiently monitoring the SOH and other states [5]. The SOH reflects the maximum available capacity and the energy supply [6-8]. The definition of SOH is generally based on capacity, internal resistance, recyclable Li-ion, and cathode solid-phase Li-ion diffusion time [9, 10]. For the pack SOH definition, Diao et al. defined it through the current pack maximum available energy and the rated pack energy [11]. The significance of SOH lies in three aspects. The first aspect is to judge the energy supply capacity and available capacity space [12]. The second aspect is to quantify the current battery economy [13]. The last aspect is to screen abnormal cells and replace degraded cells [14]. Most existing battery pack SOH estimation methods lack the engineering applicability. Hence, it is urgent to improve the estimation idea and promote its universality [15-18].

The main motivation to encourage this research is the current demand of effective energy storage based on Li-ion batteries. It reflects the impact of the work on the related research field. For this field, the most important problem is to efficiently replace degraded cells and screen abnormal cells. The developed SOH estimation method is applied to multiple working conditions, which can provide an efficient reference for the replacement of cells in new energy storage systems.

SOH obtaining approaches includes direct measurement and indirect estimation methods. Common direct measurement methods are Coulomb counting method and electrochemical impedance spectroscopy (EIS) method [19, 20]. The Coulomb counting method calculates SOH through the current and the state of charge (SOC) [21, 22]. However, the errors of this method accumulate continuously [23, 24]. The EIS method can accurately quantify the SOH by part of the internal impedance, but it requires plenty of complex experiments and a long time [25].

Indirect estimation methods are more in line with the engineering requirements. Among them, model-based methods, data-driven methods and hybrid methods are included. Model-based methods mainly consist of equivalent circuit model-based (ECM-based) and electrochemical model-based (EM-based) methods. The steps of model-based methods include model establishment, parameter identification and filtering framework construction. By analyzing complexity, accuracy and robustness of various ECMs, Hu et al. verified the first-order RC model with hysteresis effect is the most suitable ECM for lithium iron phosphate ($LiFePO_4$) battery [26]. ECM parameter identification methods involve curve fitting comparison methods, least square methods and intelligent optimization methods [15, 27]. Then, filtering algorithms are introduced. Wu et al. constructed a firefly particle filtering algorithm to estimate SOH [28]. ECMs are hard to explain internal changes, which affects the accuracy. Therefore, EM-based methods are often used in scenarios requiring more accurate estimation. Common EMs include pseudo-two-dimensional (P2D) model and its simplified models. There are two methods to simplify the P2D model. The first method is to simplify the formula expression [29, 30], and the second method is to simplify the structure or parameters [31]. Single particle (SP) model and extended single particle (ESP) model are based on the second method. Based on the SP model, Wu et al. achieved SOH estimation by analyzing the variation of Li-ion concentration difference with degradation between fully charged state and fully discharged state [32]. It is worth noting that physical models are useless in some practical cases because of its high complexity and low computational efficiency.

Common data-driven SOH estimation methods involve artificial neural network-based (ANN-based) method, support vector machine-based (SVM-based) method, fuzzy logic-based (FL-based) method, incremental capacity-based (IC-based) method, and differential voltage-based (DV-based) method [33-36]. ANN-based estimation methods include forward feedback neural network-based (FFNN-based) methods, recursive neural network-based (RNN-based) methods, deep neural network-based (DNN-based) methods and convolution neural network-based (CNN-based) methods. In RNN-based methods, the long short-term memory (LSTM) has become popular. An active state tracking-LSTM model for multi-cell sharing information was developed by Li et al. to obtain battery states [37]. Recently, CNN-based methods, SVM-based methods and IC-based methods were used for SOH estimation. For on-board SOH estimation, based on a temporal CNN,

Bockrath et al. developed an end-to-end method [38]. Gu et al. put forward a SOH estimation approach based on data pre-processing and a CNN-transformer framework [39]. Liu et al. estimated SOH using an indirect enhanced HI and the SVM [40]. He et.al performed a study on the filtering-based and the voltage-capacity model-based IC analysis methods [41].

The model-based methods are difficult to balance efficiency and accuracy. The data-driven methods strongly depend on the data quality and HIs, while some hybrid methods can complement above methods. The core idea of hybrid methods is to combine different estimation methods. Son et al. extracted multi-physics features as HIs from mechanical and electrochemical evolutionary responses [42]. A hybrid physical model was established based on the electrochemical mechanism and the traditional ECM [43]. Liu et al. combined SVM and LSTM to construct multi-feature fusion models to estimate SOH [44]. Based on the feature extraction by extremely randomized trees, Duan et al. presented an improved extreme learning machine to construct a new SOH estimation framework [45]. In the work of Jiang et al., building upon the self-attention mechanism and the automatic feature extraction method with convolutional autoencoder, a SOH estimation approach was developed [46]. Combining transfer learning and LSTM, Deng et al. formed a SOH estimation model [47]. Chen et al. proposed a SOH estimation framework with a gated recurrent unit neural network (GRUNN) [48]. However, the above hybrid methods share a common research gap by not adequately considering the applicability of the network after changes in working conditions, particularly in the case of end-to-end networks that directly incorporate voltage, current, and temperature as HIs. Changes in voltage, current, and temperature can significantly impact the relationship between these inputs and the SOH estimation, rendering the network less reliable and accurate. Therefore, within a fixed network, establishing a SOH estimation model suitable for multiple working conditions is the focus of this paper. In the future, the trend of direct measurement methods aims to achieve more accurate measurement results. The trend of model-based methods focuses on optimizing physical models and filtering algorithms. Data-driven methods and related hybrid methods are trending towards establishing estimation models with higher universality and computational efficiency.

In this research, a hybrid SOH estimation algorithm for energy storage battery packs is proposed. On the one hand, based on the ESP model, the CCPSO algorithm is used to identify the maximum solid-phase Li-ion concentrations of positive

and negative electrodes in the process of degradation. On the other hand, two degradation modes are quantified through incremental capacity-differential voltage (IC-DV) curves. The identification results and the quantitative results are regarded as HIs. Then, the strong correlation between SOH sequences and HIs is proved by grey relational analysis (GRA) and Pearson correlation analysis (PCA) methods. Finally, taking the above HIs as the input of the NSA-BP model and the SOH sequences as the output of the model, the long-term SOH estimation results can be obtained after training and testing.

The main innovation includes the following parts. Firstly, in identification, cooperation and competition strategies are introduced to optimize identification results. Secondly, the NSA algorithm is adopted to optimize the initial BP parameters. Thirdly, a quantification method for degradation modes is developed. Lastly, in the proposed method, retraining network is avoided when the working condition changes. This approach significantly enhances the universality and applicability.

The rest of this paper is arranged as follows: Section 2 makes the mathematical analysis, including ESP modeling, ESP-MCM pack modeling, CCPSO identification, IC-DV quantification, Pearson correction analysis, grey correlation analysis and NSA-BP estimation modeling. The experimental platform setup, model verification and estimation result analysis are described in detail in Section 3. Finally, Section 4 introduces the important conclusions and prospects of the full text.

2. Mathematical analysis

2.1. The establishment of ESP model and ESP-MCM

In this research, the ESP model considers the liquid-phase potential caused by concentration and ohmic polarization in liquid-phase on the SP model. The structure diagram of the ESP model is shown in Figure 1.

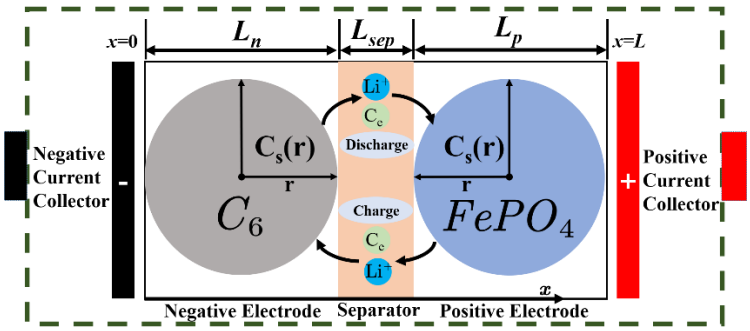

Figure 1 Structure diagram of the ESP model for energy storage Li-ion battery

In Figure 1, x, r, L_n, L_{sep}, L_p and L represent the thickness coordinate of electrodes, the radius direction of the active particles, the thickness of the negative electrode, the thickness of the separator, the thickness of the positive electrode and the thickness of the total cell. The expression of ESP model is shown in Equation (1).

$$\begin{aligned} U_t &= \varphi_{s,p}(L) - \varphi_{s,n}(0) \\ &= E_p(\theta_p) - \eta_{act,p} - \eta_{SEI,p} - \eta_{liq,p} - \left[E_n(\theta_n) - \eta_{act,n} - \eta_{SEI,n} - \eta_{liq,n} \right] \\ &= E - \eta_{act} - \eta_{SEI} - \eta_{liq} \end{aligned} \tag{1}$$

Among them, U_t and E are the terminal voltage and the open-circuit potential, $\varphi_{s,i}$ and E_i signify the solid-phase potential and the open-circuit potential of electrode i, $\eta_{act,i}$ and $\eta_{SEI,i}$ are the reaction polarization potential and ohmic polarization potential of electrode i, η_{act} and η_{SEI} denote the reaction polarization overpotential and ohmic polarization overpotential, and θ_i means the utilization rate of electrode i. E is expressed in Equation (2).

$$\begin{cases} E = E_p(\theta_p) - E_n(\theta_n) \\ \theta_p = \dfrac{c_{s,surf,p}}{c_{s,\max,p}}, \theta_n = \dfrac{c_{s,surf,n}}{c_{s,\max,n}} \end{cases} \tag{2}$$

Among them, $c_{s,surf,i}$ and $c_{s,max,i}$ denote the surface solid-phase Li-ion concentration and the maximum solid-phase Li-ion concentration of electrode i, respectively. Based on the construction principle of ESP model, the expression of j_i at the boundary of electrode collector is shown in Equation (3).

$$j_i = \frac{I}{a_s F L_i A_i}, a_s = \frac{3\varepsilon_{s,i}}{R_{s,i}} \tag{3}$$

Among them, I is the working current, a_s is the surface area of spherical active particles per unit volume, F is Faraday constant, A_i is the effective area of electrode i, $R_{s,i}$ is the radius of the particle, and $\varepsilon_{s,i}$ is the solid-phase volume fraction. Based on the previous research [14], The expressions of η_{act} and η_{SEI} are shown in Equation (4).

$$\begin{cases} \eta_{act,i} = \dfrac{2RT}{F} \ln\left(m_i + \sqrt{m_i^2 + 1} \right) \\ m_i = \dfrac{j_i}{2k_i \left(c_{s,\max,i} - c_{s,surf,i}(t) \right)^{0.5} \left(c_{s,surf,i}(t) \right)^{0.5} c_e^{0.5}} \\ \eta_{SEI} = \eta_{SEI,n} - \eta_{SEI,p} = R_{SEI,n} F j_n - R_{SEI,p} F j_p \end{cases} \tag{4}$$

Among them, R, T, k_i and c_e denote the universal gas constant, the average temperature, the average electrode reaction rate constant and the liquid-phase Li-ion concentration. The expression of η_{liq} is shown in Equation (5).

$$\eta_{liq} = \eta_{liq,n} - \eta_{liq,p} = \eta_{con-pol,n} - \eta_{con-pol,p} + \eta_{liq-ohm,n} - \eta_{liq-ohm,p} = \eta_{con-pol} + \eta_{liq-ohm} \quad (5)$$

Among them, all overpotentials are described in liquid-phase, and i represents the electrode i. $\eta_{con\text{-}pol}$ is the concentration polarization overpotential, and $\eta_{liq\text{-}ohm}$ is the ohmic polarization overpotential. The reactions of liquid-phase potential distribution are shown in Equation (6).

$$\begin{cases} \dfrac{\partial \varphi_{e,i}}{\partial x} = -\dfrac{i_{e,i}}{\kappa_{eff,i}} + \dfrac{2RT}{F}\left(1-t_+\right)\dfrac{\partial \ln c_{e,i}}{\partial x} \\ \kappa_{eff,i} = \kappa_i \varepsilon_{e,i}^{1.5} \end{cases} \quad (6)$$

Among them, $\varphi_{e,i}$ is the liquid-phase potential, $i_{e,i}$ is the liquid-phase current density, κ_i and $\kappa_{eff,i}$ are the normal and effective liquid-phase Li-ion conductivity, $\varepsilon_{e,i}$ is the liquid-phase volume fraction, and t_+ is the liquid-phase Li-ion transfer coefficient. When $\eta_{liq\text{-}ohm}$ is ignored, $\eta_{con\text{-}pol}$ is obtained by Equation (6) and the Li-ion distribution difference, as shown in Equation (7).

$$\eta_{con-pol} = \frac{2RT}{F}\left(1-t_+\right)\ln\frac{c_e\left(0\right)}{c_e\left(L\right)} \quad (7)$$

To obtain $\eta_{con\text{-}pol}$, it is necessary to calculate the boundary c_e. The expressions of $c_{e,i}$ are described in the previous research [49]. When $\eta_{con\text{-}pol}$ is ignored, $\eta_{liq\text{-}ohm,i}$ is obtained by Equation (6) and the principle of charge conservation the Li-ion battery [49], as shown in Equation (8).

$$\begin{cases} \eta_{liq-ohm,n}\left(x\right) = -\dfrac{Ix^2}{L_n A_n \kappa_{eff,n}} \\ \eta_{liq-ohm,p}\left(x\right) = -\dfrac{I}{2A_n}\left(\dfrac{L_n}{\kappa_{eff,n}} + \dfrac{2L_{sep}}{\kappa_{eff,sep}} + \dfrac{\left(x-L_n-L_{sep}\right)^2}{L_p \kappa_{eff,p}}\right) \end{cases} \quad (8)$$

As $\eta_{liq\text{-}ohm}$ is the difference between $\eta_{liq\text{-}ohm,p}$ and $\eta_{liq\text{-}ohm,n}$, the expression of $\eta_{liq\text{-}ohm}$ is expressed in Equation (9).

$$\eta_{liq-ohm} = \frac{I}{2A_n}\left(\frac{L_n}{\kappa_{eff,n}} + \frac{2L_{sep}}{\kappa_{eff,sep}} + \frac{L_p}{\kappa_{eff,p}}\right) \quad (9)$$

Therefore, combined with the definition of terminal voltage, open-circuit voltage expression and various overpotential expressions, the terminal voltage of the proposed ESP model is demonstrated in Equation (10).

$$U_t = E_p(\theta_p) - E_n(\theta_n) - \frac{2RT}{F}\frac{\ln\left(m_n + \sqrt{m_n^{\,2}+1}\right)}{\ln\left(m_p + \sqrt{m_p^{\,2}+1}\right)} - \left(R_{SEI,n}Fj_n - R_{SEI,p}Fj_p\right) - \left[\frac{2RT}{F}(1-t_+)\ln\frac{c_e(0)}{c_e(L)} + \frac{I}{2A_n}\left(\frac{L_n}{\kappa_{eff,n}} + \frac{2L_{sep}}{\kappa_{eff,sep}} + \frac{L_p}{\kappa_{eff,p}}\right)\right] \tag{10}$$

Equation (10) is the fitting terminal voltage output expression of the ESP model. Its structure block diagram is illustrated in Figure 2.

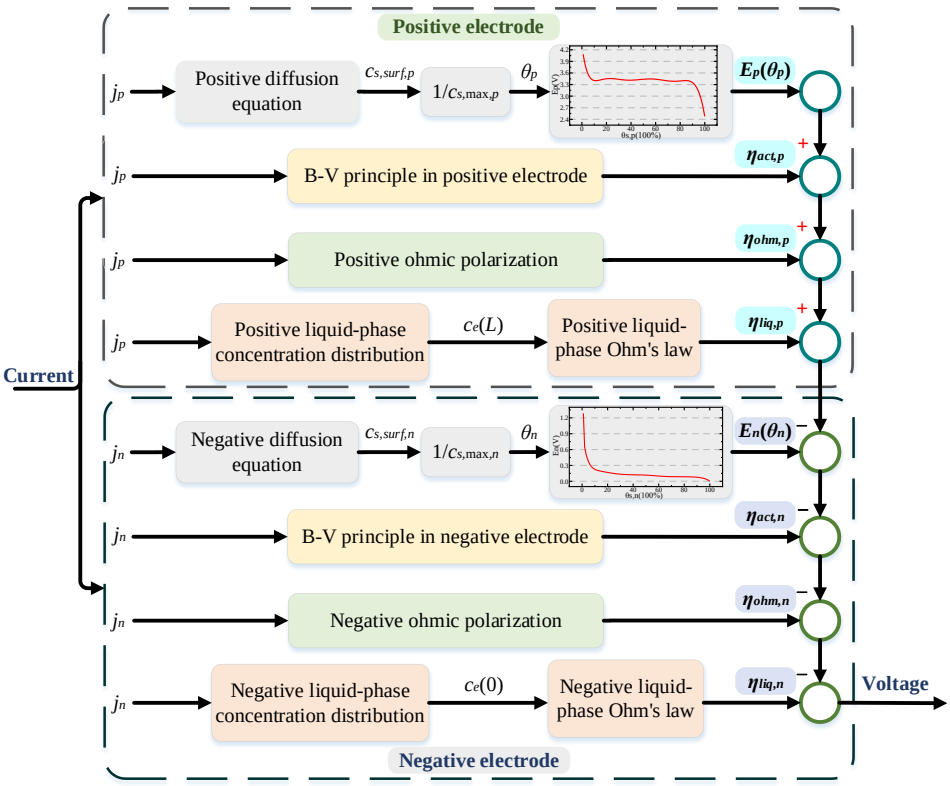

Figure 2 The structure block diagram of the ESP model

It can be known from Figure 2 that the structure block diagram involves two modules. Two graphs included in modules show the curve changes of positive and negative open-circuit voltages. Based on the ESP model, a pack model named ESP-MCM is proposed. It can meet the separate identification of electrochemical parameters in each cell. Its structure diagram is shown in Figure 3.

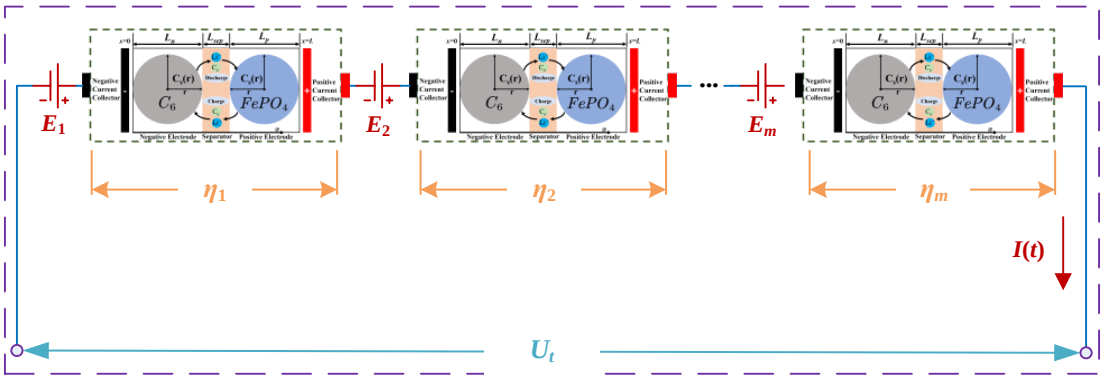

Figure 3 The structure diagram of the ESP-MCM

In Figure 3, E_m is the open-circuit voltage of the m-th cell, η_m is the sum of all the overpotentials of the m-th cell, I is the current through the series battery pack, and U_t is the whole terminal voltage. According to Equation (1), the terminal voltage expression of the m-th cell in the ESP-MCM is shown in Equation (11).

$$\begin{cases} U_{t,m} = E_m - \eta_m \\ \eta_m = \eta_{act,m} + \eta_{SEI,m} + \eta_{liq,m} \end{cases} \tag{11}$$

Among them, m represents the m-th cell. The terminal voltage of the pack model is shown in Equation (12).

$$U_t = \sum_{m=1}^{n} U_{t,m} \tag{12}$$

Among them, n denotes the cell number in a pack. Because the proposed ESP-MCM proposed is based on series structure, the pack terminal voltage is the accumulation of the individual terminal voltages.

2.2. CCPSO parameter identification algorithm

The end-to-end model with fixed network parameters is usually only suitable for one working condition, which is hard to efficiently demonstrate the relationship between HIs and SOH when the working condition changes [14, 50, 51]. In the EM, $c_{s,max,p}$ and $c_{s,max,n}$ are directly related to the SOH. Therefore, in this research, they are used as HIs. In standard PSO algorithm, the updating process of the speed and position in this algorithm is explained in Equation (13).

$$\begin{cases} v_{i,d}(k+1) = wv_{i,d}(k) + c_1 r_1 \left(p_{best,i,d}(k) - x_{i,d}(k) \right) + c_2 r_2 \left(g_{best,d}(k) - x_{i,d}(k) \right) \\ w = w_{\max} - \dfrac{w_{\max} - w_{\min}}{k_{iter}} k \\ x_{i,d}(k+1) = x_{i,d}(k) + v_{i,d}(k+1) \\ X_i = \left(x_{i,d}, x_{i,2}, \cdots x_{i,D} \right)^T, V_i = \left(v_{i,1}, v_{i,2}, \cdots v_{i,D} \right)^T \\ p_{best,i} = \left(p_{best,i,1}, p_{best,i,2}, \cdots p_{best,i,D} \right), g_{best} = \left(g_{best,1}, g_{best,2}, \cdots g_{best,D} \right) \end{cases} \tag{13}$$

Among them, *d* denotes the *d*-dimension, *i* denotes the *i*-th particle, *v* denotes the speed, *x* denotes the position, p_{best} denotes the current individual optimal solution, g_{best} denotes the current population optimal solution, and *V* denotes the speed set. In addition, w_{max} is the maximum value of weight factor, w_{min} is the minimum value of weight factor, *k* is the current number of iterations, k_{iter} is the maximum number of iterations, *X* is the position set, r_1 and r_2 are random numbers in 0 to 1, c_1 and c_2 are learning factors, and *D* is the search space dimension.

The standard PSO algorithm cannot provide the evolutionary diversity of particle swarm. Hence, the CCPSO algorithm is proposed by introducing cooperation and competition strategies. They increase the evolutionary diversity by expanding population categories and search methods, respectively.

The cooperation strategy divides the evolutionary regions of particle swarm, so that each subpopulation can evolve towards different methods. During each evolution of the population, each subpopulation exchanges information with a designed communication frequency function, which is expressed in Equation (14).

$$\begin{cases} f(t) = rand(0,1), \quad F(t) = \dfrac{k}{k_{iter}} \\ f(t) < F(t) \end{cases} \tag{14}$$

Among them, $f(t)$ is a random function within 0 and 1, $F(t)$ is the communication frequency function, and *k* and k_{iter} are the current and maximum iterations. The linearly increasing communication frequency function is adopted in this paper. Particles evolve at two speeds under the competition strategy. The sub-particle with smaller fitness is retained. After introducing the competition strategy, the expressions of speed and position in Equation (13) are optimized, as shown in Equation (15).

$$\begin{cases} v_{i,d,t}(k+1) = w_t v_{i,d}(k) + c_1 r_1 \left(p_{best,i,d}(k) - x_{i,d}(k) \right) + c_2 r_2 \left(g_{best,d}(k) - x_{i,d}(k) \right) \\ x_{i,d,t}(k+1) = x_{i,d,t}(k) + v_{i,d,t}(k+1) \\ v_{i,d}(k) = \left\{ v_{i,d,t}(k) \middle| \min J\left(x_{i,t}(k) \right) \right\}, x_{i,d}(k) = \left\{ x_{i,d,t}(k) \middle| \min J\left(x_{i,t}(k) \right) \right\} \end{cases} \tag{15}$$

Among them, d is the d-dimension, i is the i-th particle, t is the sub-particle, v is the speed, w is the weight factor, x is the position, k is the iteration number, and J is the objective function. To ensure the evolutionary diversity, two speeds of each particle should be significantly different. In this research, the basic idea of parameter identification is to minimize the variance between the measured and simulation terminal voltage of the ESP model. Therefore, the objective function of parameter identification is expressed in Equation (16).

$$\min J(\theta) = \sum_{k=1}^{n} \left[V_k - f(I_k, \theta) \right]^2, \theta = \left(c_{s,\max,p}, c_{s,\max,n} \right) \tag{16}$$

Among them, k is the sampling time, V_k is the measured terminal voltage, I_k is the input current, $f(I_k, \theta)$ is the estimated terminal voltage of the ESP model, θ is the set of electrochemical parameters to be identified, and n is the maximum sampling time. It is worth noting that $f(I_k, \theta)$ is calculated by Equation (10). The flowchart of using the CCPSO algorithm to identify $c_{s,max,i}$ in the ESP model is shown in Figure 4.

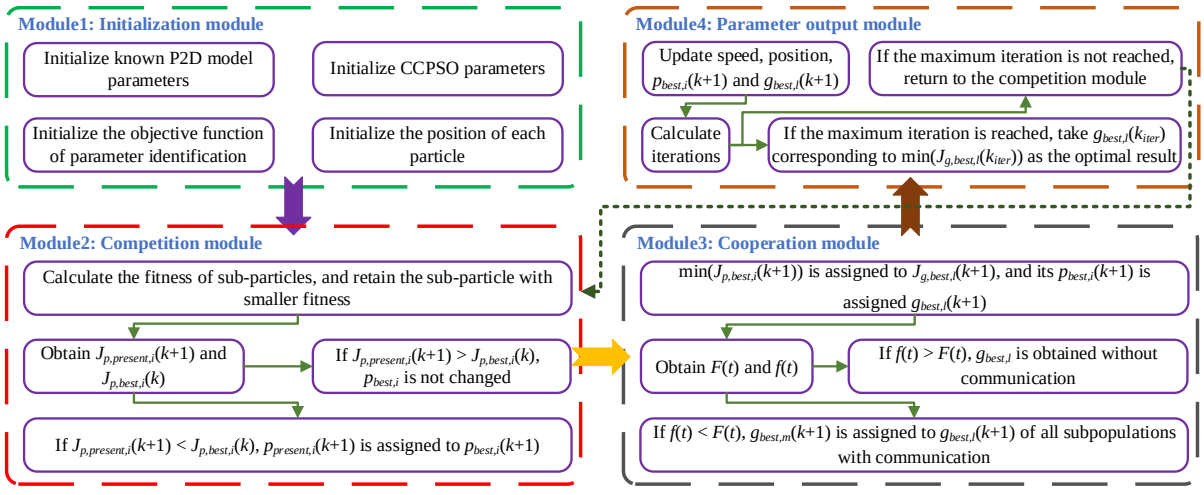

Figure 4 The flowchart of using the CCPSO algorithm for identification

In Figure 4, i denotes the i-th particle, l denotes the l-th subpopulation, m denotes the optimal subpopulation, $J_{p,present}$ and $p_{present}$ denote the fitness value and the position for a particle, and p_{best} and g_{best} denote the optimal identification results for a particle and a subpopulation. Additionally, $J_{p,best}$ and $J_{g,best}$ are the fitness of the

optimal identification results for a particle and a subpopulation.

2.3. Quantification of degradation modes based on IC-DV method

Degradation modes mainly include loss of lithium inventory (LLI), loss of active material (LAM) and conductivity loss (CL). Obvious LLI and LAM appear in degradation of Li-ion batteries. LLI and LAM can only be quantified under low-rate conditions in this paper [52]. In this research, the quantized values of LLI and LAM are adopted. The IC-DV method converts the approximately constant voltage in the open-circuit voltage curve into $\Delta Q/\Delta U$ of the IC curve and $\Delta U/\Delta Q$ of the DV curve. By observing the changes of IC-DV curves, the relationship between the external and internal characteristics is established. The expressions of the IC-DV method are shown in Equation (17).

$$IC = \frac{\Delta Q}{\Delta U}, DV = \frac{\Delta U}{\Delta Q} \tag{17}$$

For obtaining the IC-DV curves, it is necessary to carry out a low-rate test. Based on the explanation of the relationship between degradation modes and IC-DV curves by relevant researchers [52-54], a quantification method of LAM and LLI is developed, as shown in Equation (18).

$$LAM = \left| \frac{\frac{\Delta Q_{IC}}{\Delta U_{IC}} - \frac{\Delta Q_{IC}}{\Delta U_{IC}}|1}{\frac{\Delta Q_{IC}}{\Delta U_{IC}}|1} \right|, LLI = \left| \frac{Q_{DV} - Q_{DV,1}}{Q_{DV,1}} \right| \tag{18}$$

Among them, $\Delta Q_{IC}/\Delta U_{IC}$ and $\Delta Q_{IC}/\Delta U_{IC}|1$ are the present peak and initial peak of the most obvious left IC curve peak. Q_{DV} and $Q_{DV,1}$ are the present capacity and initial capacity of the most obvious DV curve peak. Figure 5 shows the quantification schematic diagrams of *Cell*2. The specific description of *Cell*2 is elaborated in Section 3.1.

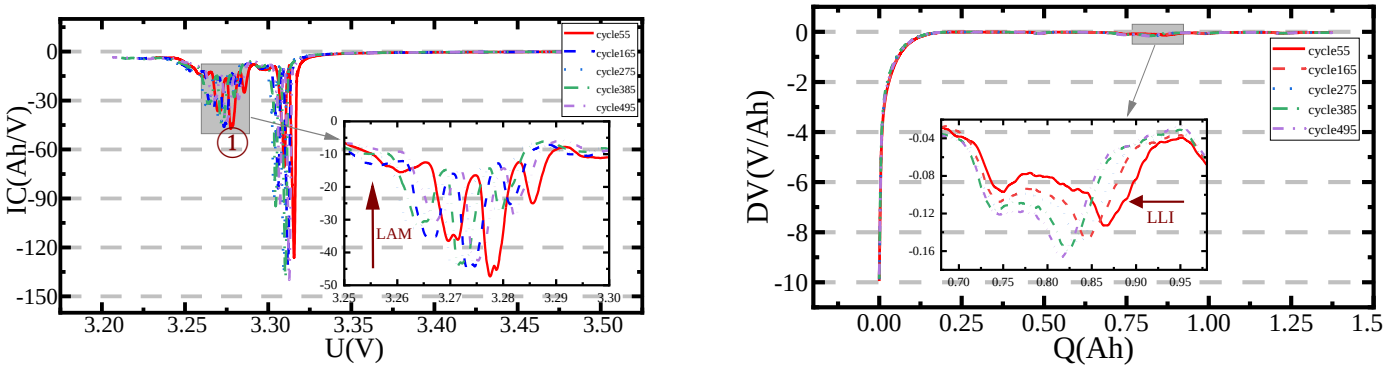

(A) LAM quantification diagram based on IC curves

(B) LLI quantification diagram based on DV curves

Figure 5 The quantification schematic diagrams of LAM and LLI

Peak 1 marked in Figure 5(A) is the most obvious peak in the left side of the IC curve. As can be seen from Figure 5, as the battery degrades, IC and LAM of Peak 1 show an upward trend, while DV and LLI of the most obvious peak in the DV curve show a downward trend and a left-shift trend, respectively.

2.4. Pearson correlation analysis and grey relation analysis methods

PCA and GRA methods are introduced to analyze the correlation. PCA method analyzes the linear correlation between the two variables by calculating the Pearson correlation coefficient, which is shown in Equation (19).

$$\rho_{X,Y}=\frac{\operatorname{cov}(X,Y)}{\sigma_X\sigma_Y}=\frac{E\left((X-\mu_X)(Y-\mu_Y)\right)}{\sigma_X\sigma_Y}=\frac{E(XY)-E(X)E(Y)}{\sqrt{E\left(X^2\right)-E^2(X)}\sqrt{E\left(Y^2\right)-E^2(Y)}} \tag{19}$$

Among them, X and Y are SOH and HI, and ρ is the Pearson correlation coefficient, which is not sensitive to nonlinear relationship [14]. Therefore, the GRA method is adopted to complement the nonlinear relationship. It quantifies the relational degree by comparing curve similarity. Its calculation framework is shown in Figure 6.

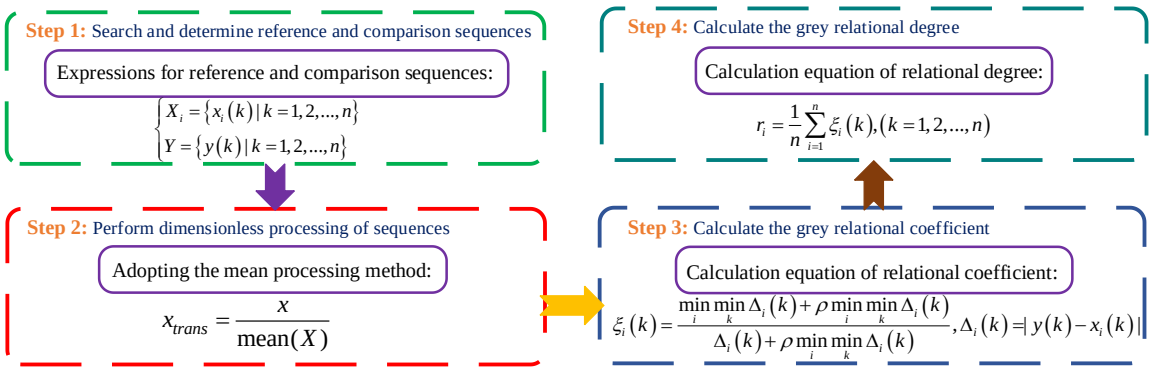

Figure 6 The calculation framework of the GRA method

In Figure 6, i is the sequence of one type of HI, k is the sequence number of this HI, n is the sequence length of k, x is a value in the sequence, x_{trans} is the sequence value of x after mean processing, ξ is the relational coefficient at each point between the sequences, ρ is the resolution coefficient, and r is the relational degree.

2.5. NSA-BP estimation modeling

The simulated annealing (SA) algorithm takes the lowest temperature of the system as the optimal solution of the objective function. In the process of optimization, this algorithm can avoid the local optimization as much as possible by introducing the escape probability. The basic framework of the SA algorithm is shown in Figure 7.

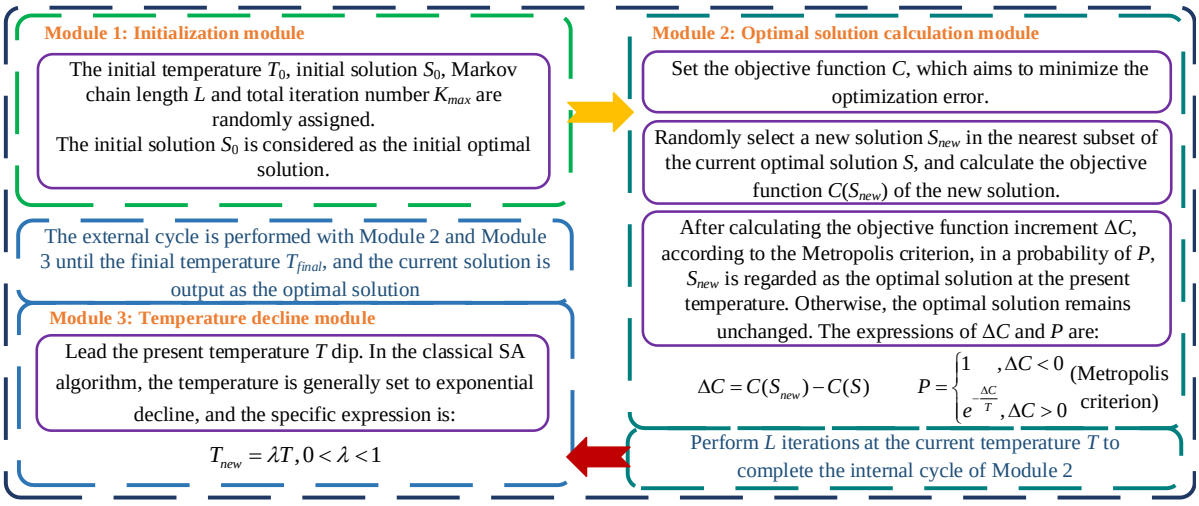

Figure 7 The basic framework of the SA algorithm

In Figure 7, λ is the temperature drop rate, T_{new} is the temperature after updating. The exponential annealing strategy is commonly used in classical SA algorithms. Its schematic diagram is shown in Figure 8(A).

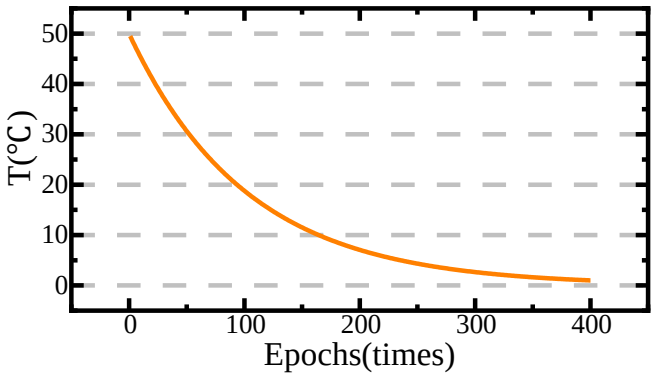

(A) The schematic diagram of the exponential annealing process

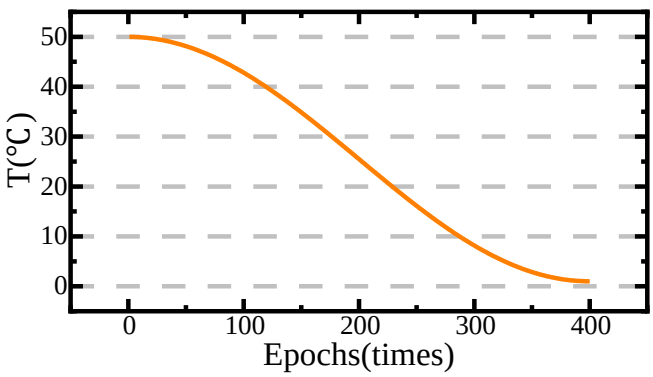

(B) The schematic diagram of the proposed annealing process

Figure 8 Schematic diagrams of two annealing processes

As shown in Figure 8(A), the change rate of the exponential annealing strategy at the initial stage is too large, which is difficult to obtain the optimal solution at this stage. To address this issue, the exponential annealing strategy is replaced by a nonlinear coefficient temperature decreasing annealing strategy in the proposed NSA algorithm. Its expression is shown in Equation (20).

$$T_{new} = \frac{T_0 - T_{final}}{2} \cos\frac{\pi}{K_{\max}} K + \frac{T_0 + T_{final}}{2} \tag{20}$$

Among them, K and K_{max} are the current and maximum iterations. The schematic diagram of nonlinear coefficient temperature decreasing annealing is shown in Figure 8(B). As can be seen from Figure 8(B), the proposed annealing curve is beneficial to explore the optimal solution at a higher temperature as well as to find the global optimal solution. For improving the computational efficiency, the BP network with a simple structure is adopted. The structure schematic diagram of a three-layer BP model is shown in Figure 9.

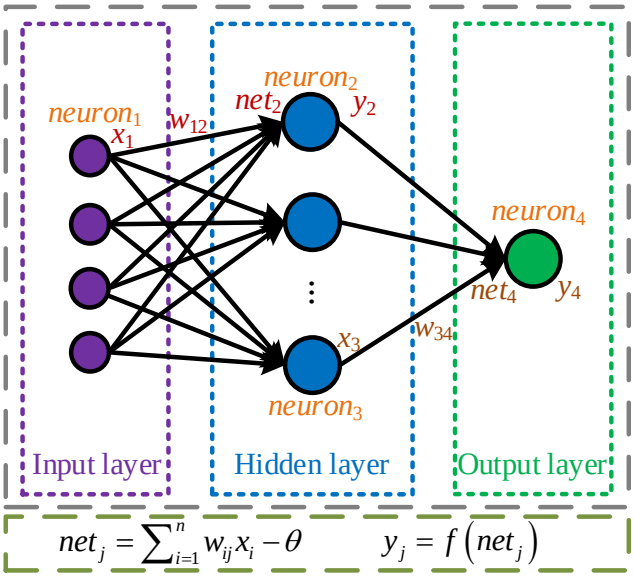

Figure 9 The structure schematic diagram of a three-layer BP neural network

In Figure 9, x_i and w_{ij} denote the signal and the weight factor. Besides, n denotes the neuron number, θ denotes the threshold, net_j denotes the input, $f()$ denotes the activation function, and y_j denotes the output. After each forward propagation process, there are errors between the model output $y_{BP,\,k}$ and the actual output $y_{t,\,k}$. The square error function is adopted as the objective function, which is elaborated in Equation (21).

$$E = \frac{1}{2}\sum_{k=1}^{N}\left(y_{t,k} - y_{BP,k}\right)^2 \tag{21}$$

Among them, E is the network error, k is the number of neurons in the output layer, and N is the total number of neurons in the output layer. The main function of the NSA algorithm is to optimize the initial parameters of BP neural network and take optimized parameters as the new start for BP network training. The flowchart of the NSA-BP algorithm is shown in Figure 10.

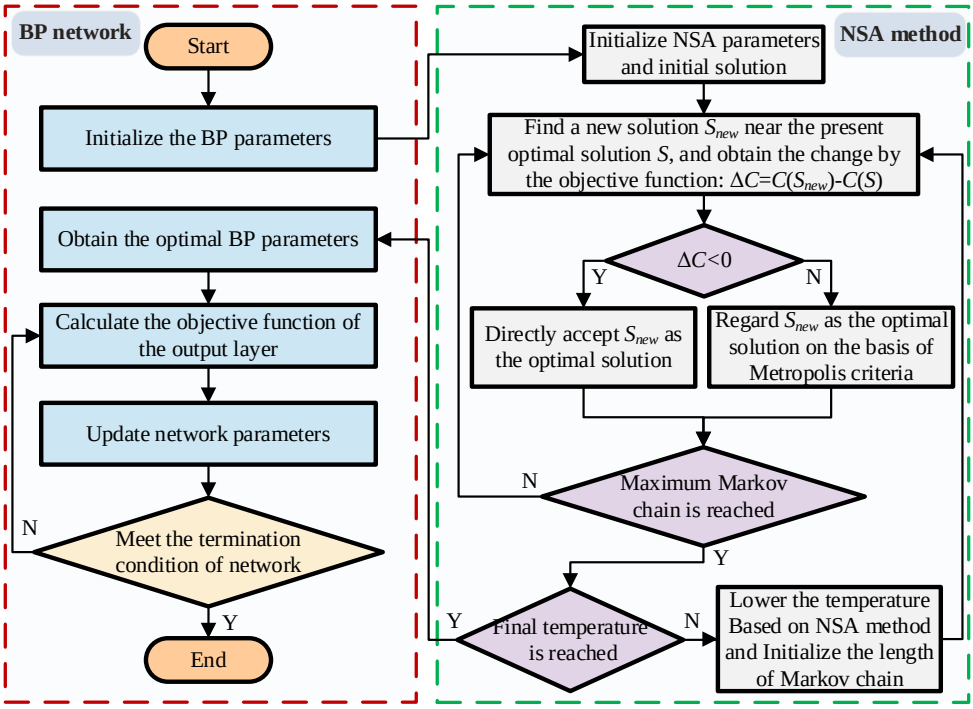

Figure 10 The flowchart of the NSA-BP algorithm

In order to study the SOH estimation model, it is necessary to determine the definition method of battery SOH. In this paper, the capacity definition method of SOH estimation is selected, as shown in Equation (22).

$$SOH = \frac{Q}{Q_{rate}} \tag{22}$$

Among them, Q and Q_{rate} represent the current capacity and the rated capacity, respectively. The network parameters are obtained by taking the SOH as the NSA-BP model output and the HIs as the model input. According to literature [55, 56], this paper defines the SOH of the Li-ion battery pack as Equation (23).

$$SOH_p = \min\left(SOH_1, SOH_2, \cdots, SOH_n\right) \tag{23}$$

Among them, n, SOH_n and SOH_p represent the cell number, the SOH of the n-th cell and the pack SOH,

respectively. The flowchart of pack SOH estimation based on the proposed model is shown in Figure 11.

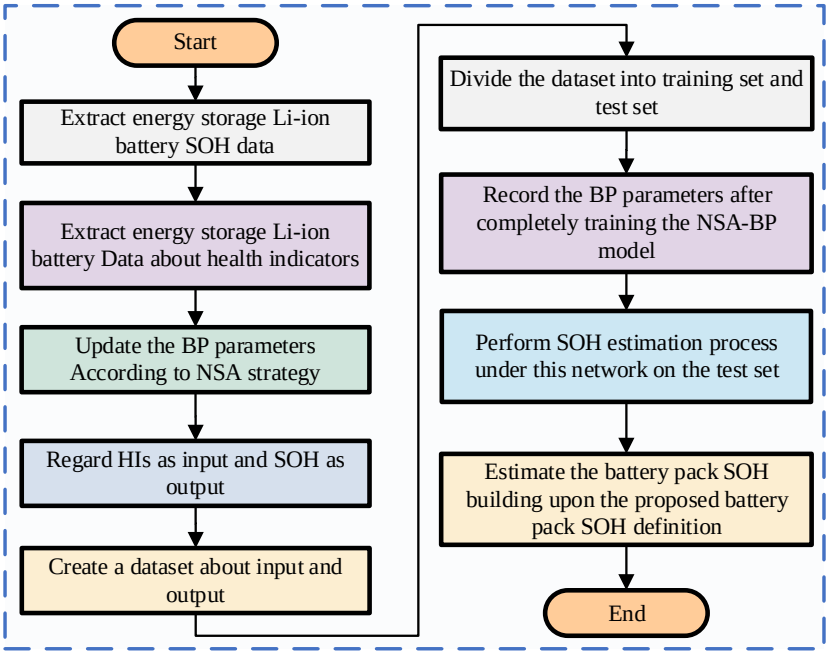

Figure 11 The flowchart of pack SOH estimation based on the improved NSA-BP network

Combined with cell model, pack model, CCPSO parameter identification algorithm, quantification method of degradation modes based on IC-DV curves, two correlation analysis methods, NSA-BP neural network model and SOH definition, the proposed SOH estimation framework of battery packs is shown in Figure 12.

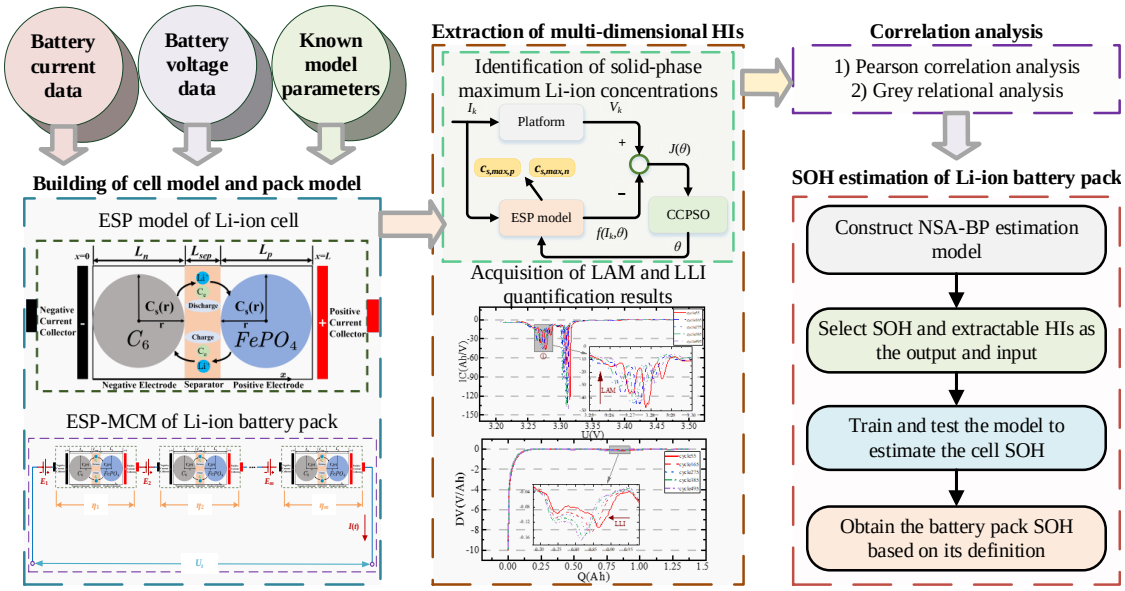

Figure 12 The proposed SOH estimation framework of energy storage battery packs

From Figure 12, it can be observed that the developed SOH estimation method considers both

electrochemistry and degradation. Specifically, the establishment of ESP model lays the foundation for the CCPSO algorithm to accurately identify $c_{s,max,i}$. In the CCPSO algorithm, the input is the battery current and known parameters in the ESP model, and the output is the values of $c_{s,max,i}$. In the IC-DV method, the input is the open-circuit voltage and discharge capacity, and the output is the quantified values of LAM and LLI. Regarding $c_{s,max,p}$, $c_{s,max,n}$, LAM and LLI as HIs, PCA and GRA methods are used to analyze the correlation between HIs and SOH. Then, HIs are adopted as the input of the NSA-BP model for network training and testing to output the estimated SOH.

3. Experimental analysis

3.1. Experimental platform and setup

In this experiment, each cell is a brand-new 26650 $LiFePO_4$ battery with rated capacity of about 2.3 Ah, upper cutoff voltage of 3.6 V and lower cutoff voltage of 2.5 V. All experiments are performed in a battery charge-discharge tester and a thermostat. The temperature of thermostat is set to 25 °C, and the output of experimental instrument is stored in computer. The computer is configured with Intel (R) Core (TM) i5-9500 and NVIDIA GeForce GT 710. The structure of test platform is shown in Figure 13.

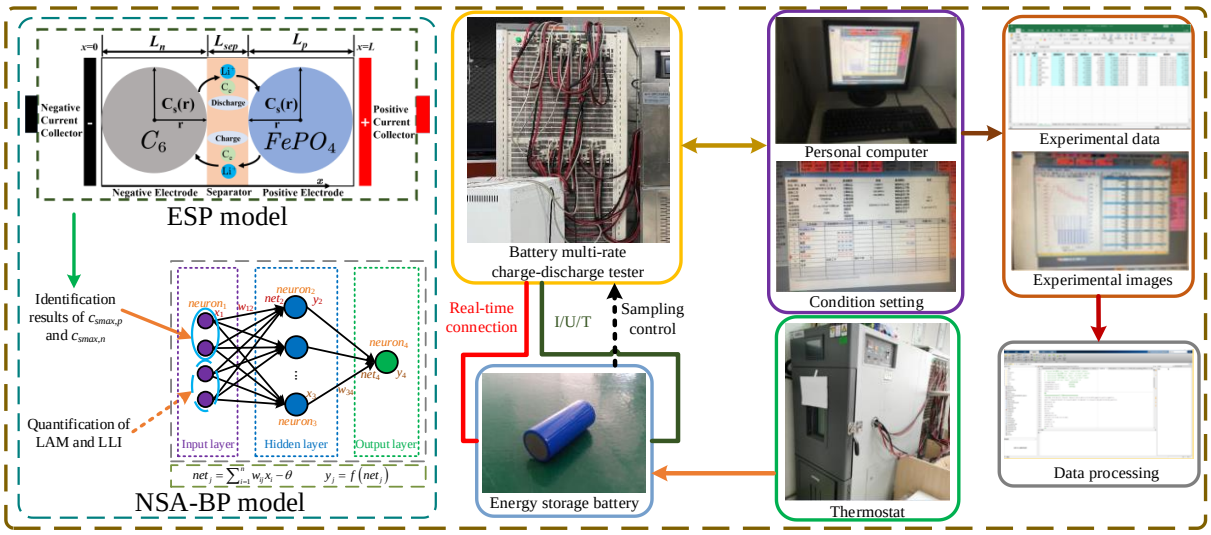

Figure 13 The structure of test platform

The experiments involve the 0.1 C full charge-discharge experiment of a cell, the 0.4 C degradation

experiment of a cell, the 0.5 C degradation experiment of a battery pack and the variable-rate degradation experiment of a battery pack. In this research, C is used to represent the charge-discharge rate of the battery. Among them, each pack is series-connected by four cells. Actually, the studied SOH estimation strategy is general for more types of lithium batteries. However, because of limitations in the current laboratory facilities, this research only used $LiFePO_4$ 26650 cells as the experimental subjects for analysis. Future work will extend to conduct comparative analysis for batteries of diverse types.

The cell at 0.1 C is called *Cell*1, the cell at 0.4 C is called *Cell*2, the battery pack at 0.5 C is called *Pack*1, and the battery pack at variable rate is called *Pack*2. Among them, *Cell*1 is used for obtaining the positive open-circuit potential expression, and *Cell*2 is used for training the SOH estimation model. In addition, *Pack*1 and *Pack*2 are used for testing the SOH estimation model. In one cycle, the current curves of *Cell*2, *Pack*1 and *Pack*2 are shown in Figure 14.

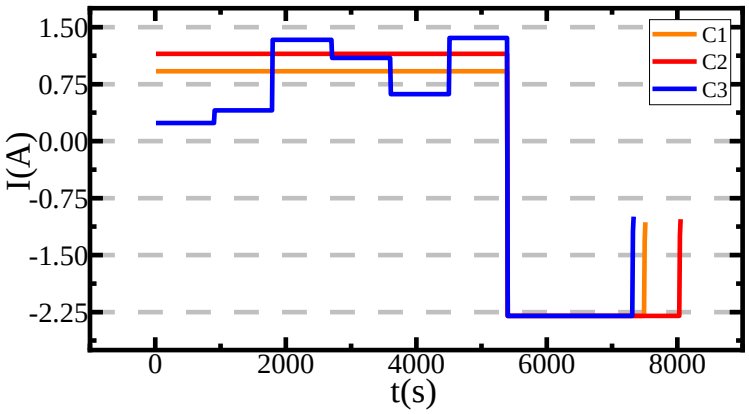

Figure 14 The current curves in each degradation cycle

In Figure 14, during the discharge process, *C*1, *C*2 and *C*3 are 0.4 C condition, 0.5 C condition and variable-rate condition, respectively. In the existing data set, the degradation conditions are both low-rate full charge-discharge conditions. In these conditions, the maximum available capacity of each cycle is calculated by current and time. However, *Cell*2, *Pack*1 and *Pack* 2 are not operating under these conditions, so the maximum available capacity in each cycle cannot be calculated. Thus, *Cell*2, *Pack*1 and *Pack* 2 need to carry out the

capacity test every about five days to obtain the maximum available capacity.

3.2. Extraction results and correlation analysis results of health indicators

The specific expressions of positive and negative open-circuit potentials are the premise of establishing ESP model. The negative open-circuit potential is expressed by empirical expression [57], and the positive open-circuit voltage expression is obtained by fitting the difference between the simulated voltage and the measured voltage of *Cell*1. The open-circuit potential of electrodes is expressed in Equation (24).

$$\begin{cases} E_n(\theta_n) = 0.6379 + 0.5416e^{-305.5309\theta_n} + 0.044\tanh\left(\frac{-(\theta_n - 0.1958)}{0.1088}\right) - 0.1978\tanh\left(\frac{\theta_n - 1.0571}{0.0854}\right) \\ -0.6875\tanh\left(\frac{\theta_n + 0.0117}{0.0529}\right) - 0.0175\tanh\left(\frac{\theta_n - 0.5692}{0.0875}\right) \\ E_p(\theta_p) = 509.0485\theta_p^{\ 8} - 2584.6784\theta_p^{\ 7} + 5232.1118\theta_p^{\ 6} - 5526.4540\theta_p^{\ 5} + 3311.6219\theta_p^{\ 4} \\ -1138.2716\theta_p^{\ 3} + 214.7627\theta_p^{\ 2} - 19.7519\theta_p + 4.0857 \end{cases} \tag{24}$$

According to Equation (24), the relationships between the open-circuit potentials of two electrodes and the utilization rate of two electrodes for energy storage Li-ion battery can be obtained, as shown in Figure 15.

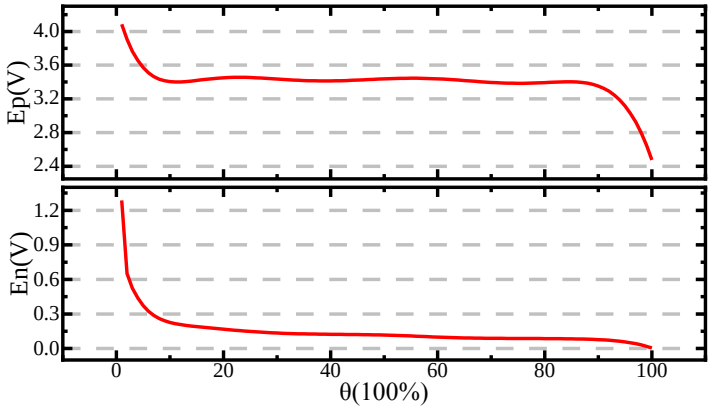

Figure 15 Positive and negative open-circuit potentials curves

In addition to the open-circuit potential expressions of electrodes, some constants and parameters need to be obtained to construct the ESP model. The known constants and parameters of ESP model are shown in Table 1.

Table 1 The known related constants and parameters of ESP model

Parameter	Notation	Value at 25℃(unit)
Faraday constant	F	96487 (C/mol)
Universal gas constant	R	8.314 (J/mol/K)
Liquid-phase Li-ion migration coefficient	t_+	0.363 (/)
Battery temperature	T	298.15 (K)
Liquid-phase Li-ion conductivity	$\kappa_p/\kappa_n/\kappa_{sep}$	0.265/0.183/0.168 (/)
Plate thickness	$L_p/L_n/L_{sep}$	$70\times10^{-6}/34\times10^{-6}/16\times10^{-6}$ (m)
Effective area of pole piece	A_p/A_n	0.17/0.17 (m^2)
The radius of the active particle	$R_{s,p}/R_{s,n}$	$3.65\times10^{-8}/3.5\times10^{-6}$ (m)

Solid-phase diffusion coefficient	$D_{s,p}/D_{s,n}$	$1.18\times10^{-18}/2\times10^{-14}$ (m^2/s)
Liquid-phase diffusion coefficient	$D_{e,p}/D_{e,n}$	$4.97\times10^{-9}/4.97\times10^{-9}$ (m^2/s)
Ohmic resistance induced by SEI film	$R_{SEI,p}/R_{SEI,n}$	0.001/0.001 ($\Omega\cdot m^2$)
Solid-phase volume fraction	$\varepsilon_{s,p}/\varepsilon_{s,n}$	0.56/0.5 (/)
Liquid-phase volume fraction	$\varepsilon_{e,p}/\varepsilon_{e,n}/\varepsilon_{e,sep}$	0.3/0.3/1 (/)
Average electrode reaction rate constant	k_p/k_n	$3\times10^{-11}/8.19\times10^{-12}$ ($m^{2.5}mol^{-0.5}s^{-1}$)
Initial liquid-phase Li-ion concentration	$c_{e,0,p}/c_{e,0,n}$	1000/1000 (mol/m^3)
Initial surface solid-phase Li-ion concentration	$c_{s,surf,0,p}/c_{s,surf,0,n}$	3900/14870 (mol/m^3)

In this research, two different identification algorithms are introduced to analyze the identification results of $c_{smax,p}$ and $c_{smax,n}$. The related parameter settings in above algorithms are shown in Table 2.

Table 2 Related parameters of identification algorithms

Parameter type	Notation	Value (unit)
Positive maximum solid-phase Li-ion concentration	$c_{s,max,p}$	[16000,27000] (mol/m^3)
Negative maximum solid-phase Li-ion concentration	$c_{s,max,n}$	[25000,36000] (mol/m^3)
Parameter dimension/ maximum iterations	d/ k_{iter}	2 /100 (/)
Initial particle speed	$v_{i,0}$	1000±100 (/)
Maximum weight factor in standard PSO	w_{max}/w_{min}	0.9/0.4 (/)
Maximum weight factor of the first sub-particle in CCPSO	$w_{max,1}/w_{min,1}$	0.9/0.7 (/)
Maximum weight factor of the second sub-particle in CCPSO	$w_{max,2}/w_{min,2}$	0.6/0.4 (/)
Learning factor	c_1/c_2	2/2 (/)
Category number of cooperative subpopulation	M	4 (/)
Particle swarm size in standard PSO	N_1	20 (/)
Particle swarm size in CCPSO	N_2	10 (/)

One the one hand, *Cell*1 is to help achieve the expression of positive open-circuit potential, so there is no need for follow-up analysis of *Cell*1. On the other hand, the HIs of *Cell*2, *Pack*1 and *Pack*2 are used to train and test the estimation model, so the relevant analysis results should be illustrated in detail.

In order to verify the improvement effect of the CCPSO algorithm, the standard PSO algorithm and the CCPSO algorithm are adopted to analyze the change curves of corresponding fitness values. The first cells in *Pack*1 and *Pack*2 are used for fitness analysis, and these two cells are named *Pack* 1-1 and *Pack* 2-1. In *Cell*2, *Pack*1-1 and *Pack*2-1. The fitness value curves during the first and the last degradation cycles are shown in Figure 16.

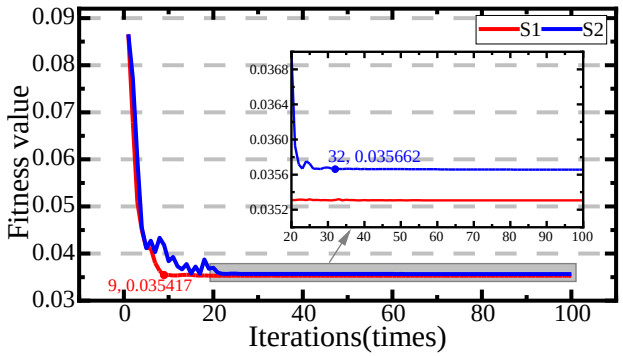

(A) Fitness analysis of *Cell*2 during the first cycle

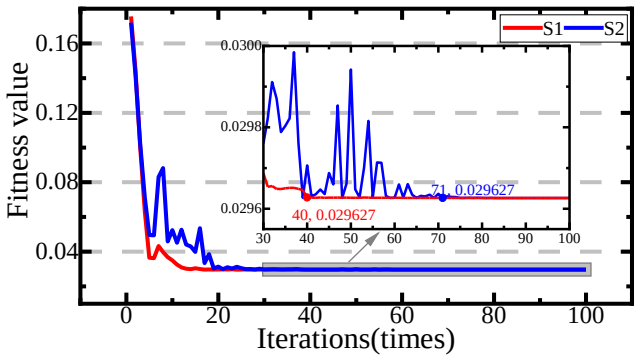

(B) Fitness analysis of *Cell*2 during the last cycle

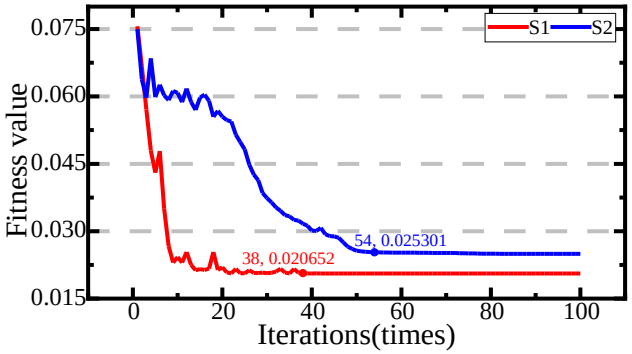

(C) Fitness analysis of *Pack*1-1 during the first cycle

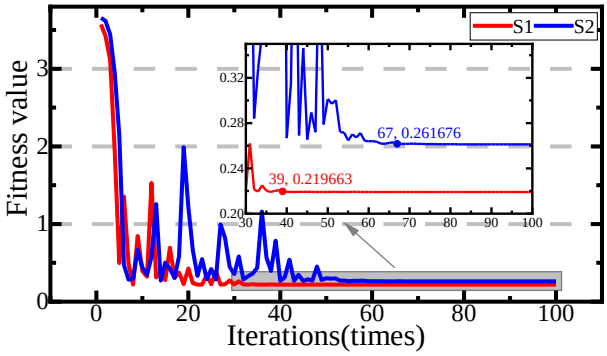

(D) Fitness analysis of *Pack*1-1 during the last cycle

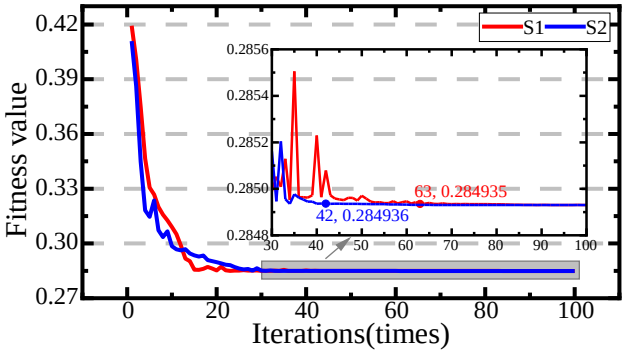

(E) Fitness analysis of *Pack*2-1 during the first cycle

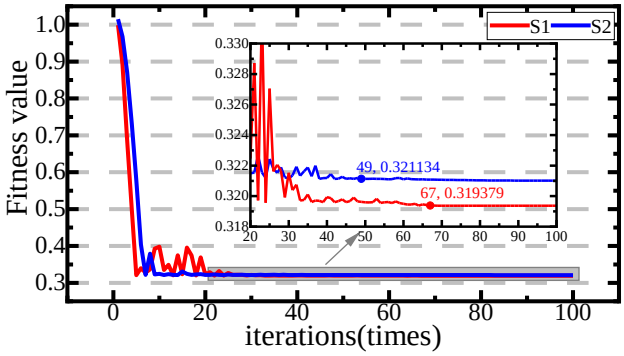

(F) Fitness analysis of *Pack*2-1 during the last cycle

Figure 16 Comparison curves of fitness value

In Figure 16, *S*1 and *S*2 denote the CCPSO and the standard PSO, respectively. It can be observed that the CCPSO algorithm converges to the optimal solution faster, and the corresponding optimal fitness value is smaller. Taking Figure 16(C) as an example, in the CCPSO algorithm and the standard PSO algorithm, the fitness value curves converge after 54 and 38 iterations, respectively, with the fitness values of 0.025301 and 0.020652, respectively, which indicates that the developed CCPSO algorithm can get rid of the local

optimization as much as possible. The above discussions verify the superiority of the CCPSO algorithm in identification accuracy and efficiency. During the SOH degradation process of the *Cell*2, *Pack*1 and *Pack*2, the parameter identification results obtained by using CCPSO algorithm are shown in Figure 17.

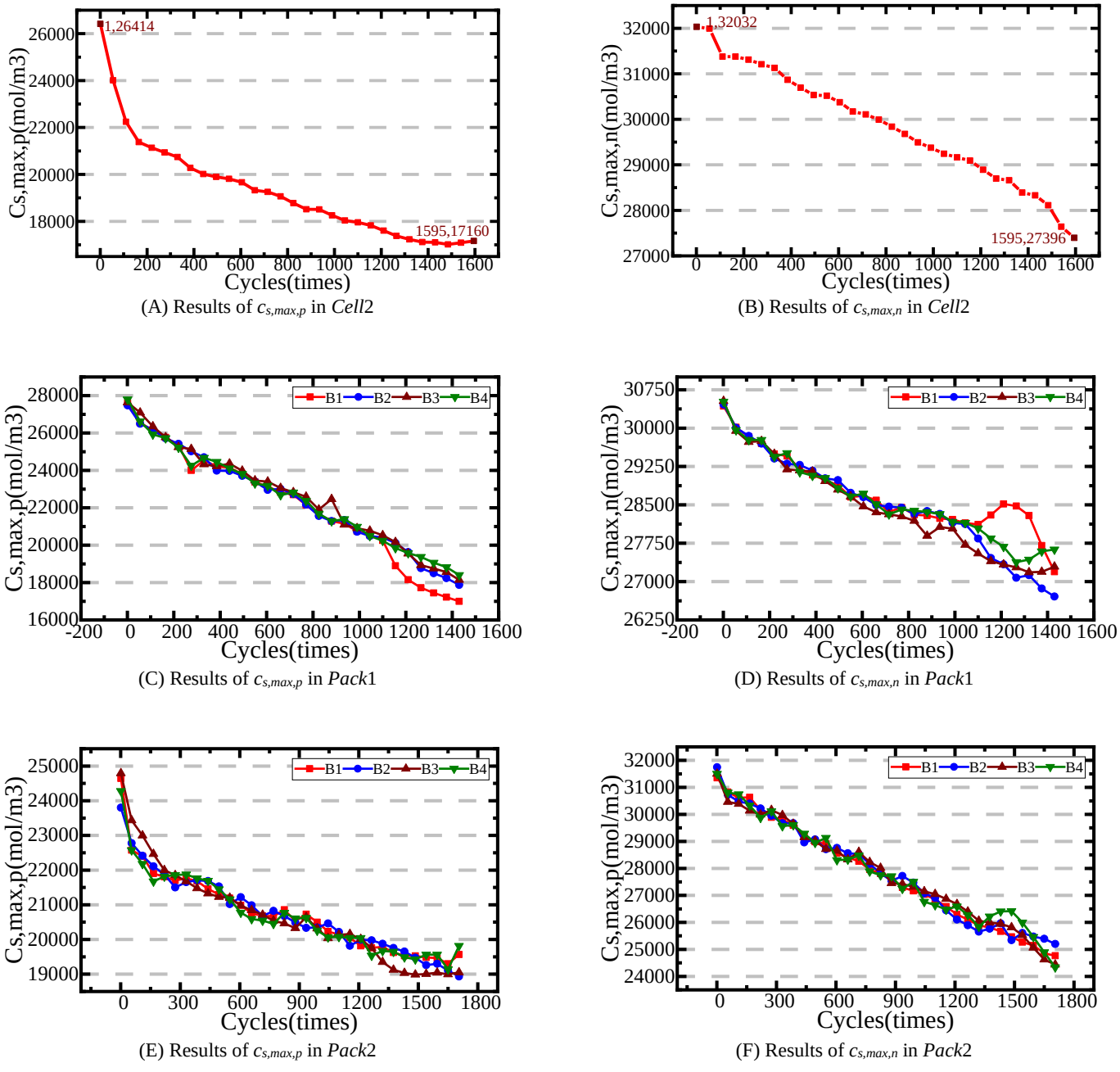

(A) Results of $c_{s,max,p}$ in *Cell*2

(B) Results of $c_{s,max,n}$ in *Cell*2

(C) Results of $c_{s,max,p}$ in *Pack*1

(D) Results of $c_{s,max,n}$ in *Pack*1

(E) Results of $c_{s,max,p}$ in *Pack*2

(F) Results of $c_{s,max,n}$ in *Pack*2

Figure 17 Results of electrochemical parameter identification

As can be seen from Figure 17, $c_{s,max,p}$ and $c_{s,max,n}$ in each cell both demonstrate a dipping trend with the degradation. Because there is a small inconsistency among cells in one battery pack, a small diversity in the

degradation of each cell is inevitable. And the difference in the later degradation stage is significantly greater than that of in the early degradation stage.

Quantification of degradation modes require the analysis of IC-DV curves. In this research, ΔU in IC curves is adopted as 0.001 V, and ΔQ in DV curves is adopted as 0.002 Ah. It is worth noting that the IC-DV quantification method can only be used under low-rate conditions. In *Cell*2 and *Pack*1, the quantification results are shown in Figure 18.

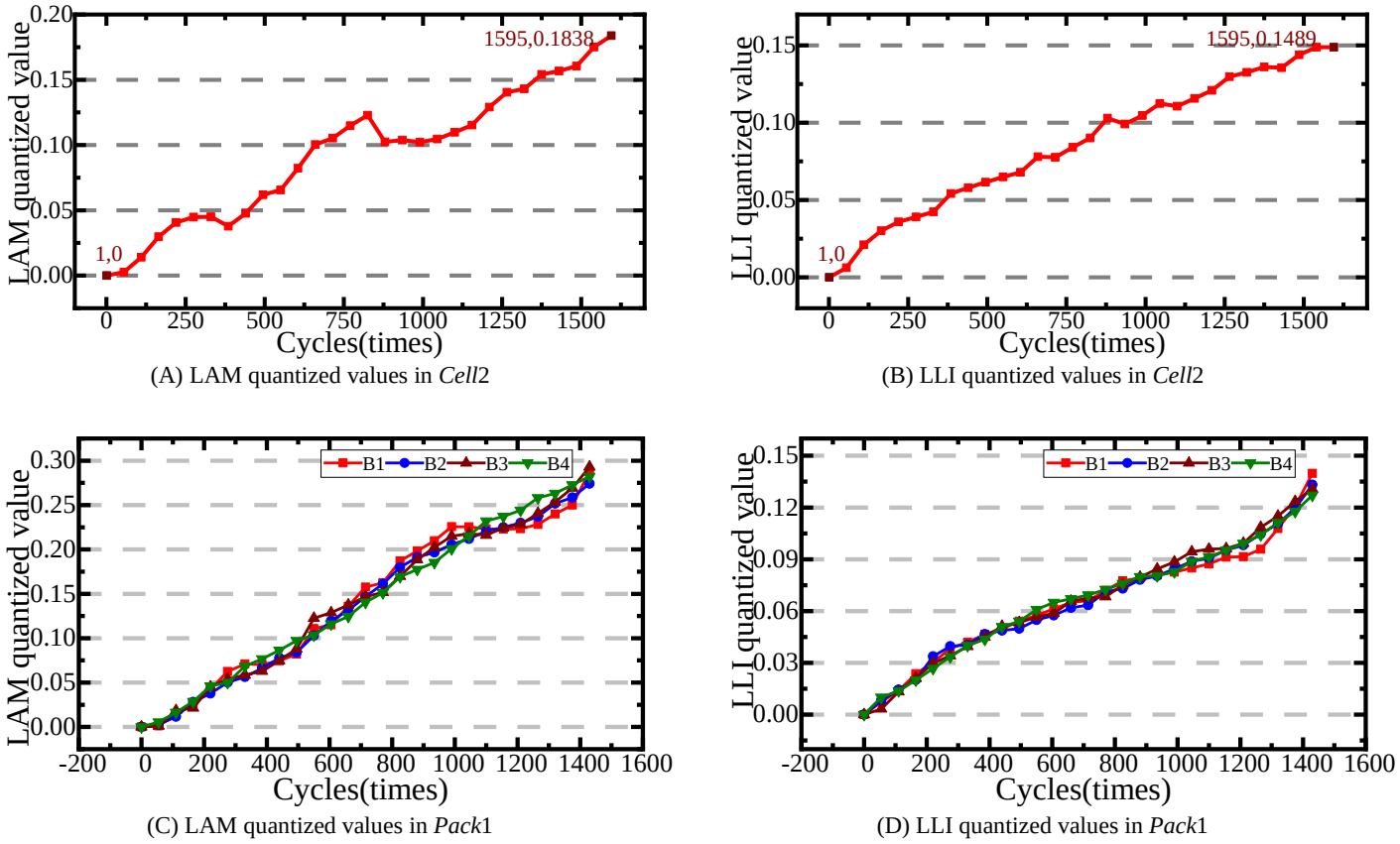

(A) LAM quantized values in *Cell*2

(B) LLI quantized values in *Cell*2

(C) LAM quantized values in *Pack*1

(D) LLI quantized values in *Pack*1

Figure 18 Quantification curves in *Cell*2 and *Pack*1

As can be observed from Figure 18, the quantification results of LAM and LLI increase with degradation. Sudden dips in LAM and LLI may reflect battery capacity recovery. Because the change trend of the quantification curves is opposite to the SOH degradation trend, the negative values of the quantification results are adopted for following analysis. The curves of capacity and SOH during the degradation for *Cell*2, *Pack*1 and *Pack*2 are illustrated in Figure 19.

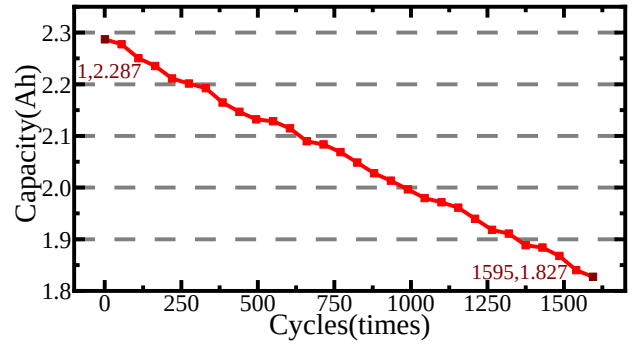

(A) The capacity of *Cell*2

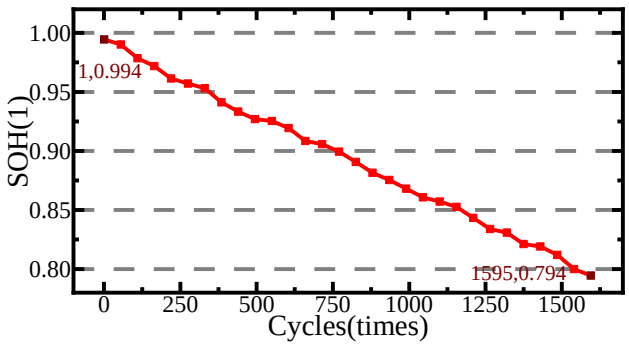

(B) The SOH of *Cell*2

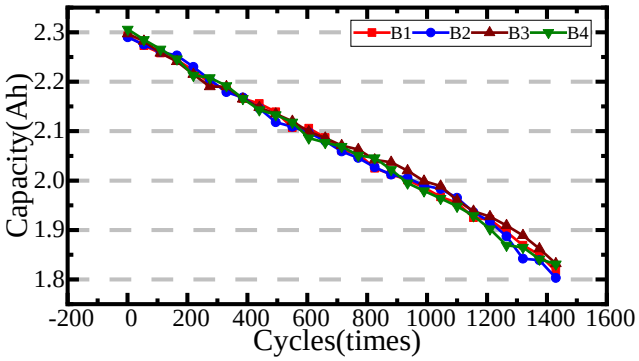

(C) The capacity of each cell in *Pack*1

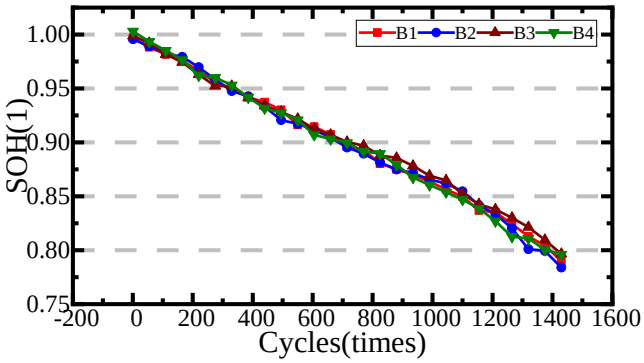

(D) The SOH of each cell in *Pack*1

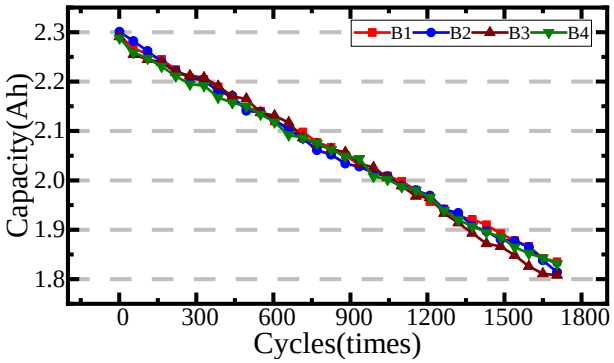

(E) The capacity of each cell in *Pack*2

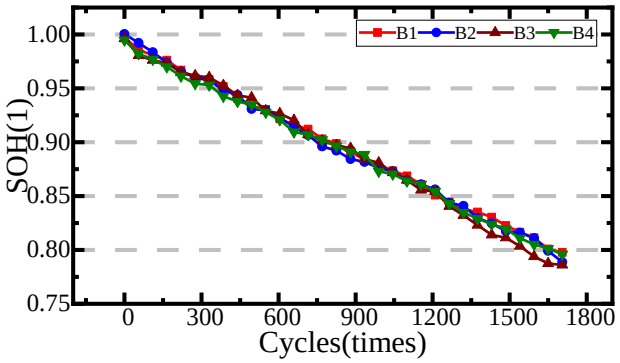

(F) The SOH of each cell in *Pack*2

Figure 19 Actual capacity curves and actual SOH curves

In this research, PCA method and GRA method are employed to analyze and evaluate the correlations between each HI and cell SOH, respectively. In *Cell*2, *Pack*1 and *Pack*2, the Pearson correlation coefficients between HIs and cell SOH are elaborated in Table 3.

Table 3 The Pearson correlation coefficients between HIs and cell SOH

Parameter	*Cell*2	*Pack*1-1	*Pack*1-2	*Pack*1-3	*Pack*1-4	*Pack*2-1	*Pack*2-2	*Pack*2-3	*Pack*2-4
$c_{s,max,p}$	0.916	0.990	0.995	0.994	0.992	0.933	0.973	0.936	0.933
$c_{s,max,n}$	0.996	0.922	0.988	0.981	0.976	0.999	0.988	0.992	0.982
LLI	0.996	0.983	0.992	0.995	0.991	/	/	/	/

LAM	0.974	0.984	0.987	0.990	0.996	/	/	/	/

In the experimental calculation and analysis, the resolution coefficient of GRA method is selected as 0.5. In *Cell*2, *Pack*1 and *Pack*2, the grey relational degrees between HIs and cell SOH are shown in Table 4.

Table 4 The grey relational degrees between HIs and cell SOH

Parameter	*Cell*2	*Pack*1-1	*Pack*1-2	*Pack*1-3	*Pack*1-4	*Pack*2-1	*Pack*2-2	*Pack*2-3	*Pack*2-4
$c_{s,max,p}$	0.502	0.775	0.600	0.738	0.681	0.532	0.587	0.516	0.553
$c_{s,max,n}$	0.849	0.553	0.622	0.466	0.526	0.876	0.634	0.813	0.828
LLI	0.767	0.711	0.705	0.790	0.720	/	/	/	/
LAM	0.821	0.771	0.679	0.792	0.824	/	/	/	/

In Table 3 and Table 4, *Packn-m* represents the *m*-th cell in the *n*-th pack. From Table 3 and Table 4, it can be seen that the correlations between four HIs and SOH sequences show different results under different working conditions, but the overall correlations are high, so the above-mentioned HIs are suitable to be used as the input of neural network for SOH estimation.

3.3. Verification of cell model under complex conditions

In this research, the cell model is verified under two low-rate conditions and a variable-rate condition, and the pack model is verified under a low-rate condition and a variable-rate condition. The cells under two low-rate conditions are modeled. Because *Cell*2 and *Pack*1 are in these working conditions, *Cell*2 and *Pack*1-1 are selected to compare and analyze the voltage fitting performance of SP model and ESP model. During the first cycle of *Cell*2 and *Pack*1-1, the actual terminal voltage and above-mentioned fitting terminal voltages are shown in Figure 20.

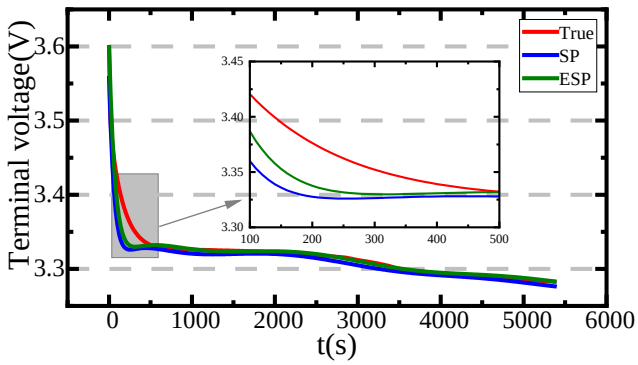

(A) The terminal voltages of *Cell*2 during the first cycle

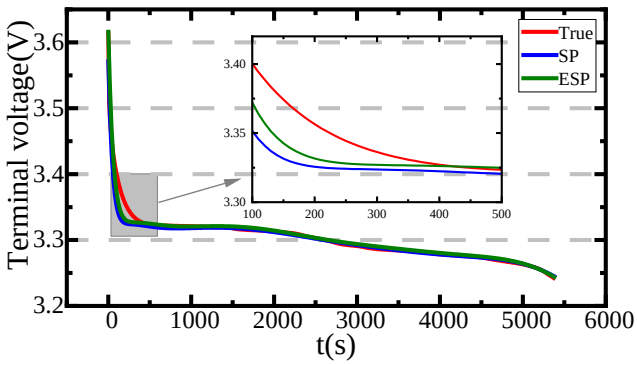

(B) The terminal voltages of *Pack*1-1 during the first cycle

Figure 20 The actual and fitting terminal voltages of *Cell*2 and *Pack*1-1 during the first cycle

Specifically, in Figure 20, the MAEs of two fitting terminal voltages are elaborated in Table 5.

Table 5 The MAEs of model fitting terminal voltages

Cell and model	*Cell*2 in SP model	*Cell*2 in ESP model	*Pack*1-1 in SP model	*Pack*1-1 in ESP model
MAE	0.00642 V	0.00359 V	0.00318 V	0.00303 V

Table 5 demonstrates the fitting performance of ESP model is better under the low-rate cyclic conditions. In addition, *Cell*2 and *Pack*1-1 are selected to verify the ESP model under low-rate cyclic conditions. The actual and fitting terminal voltages during the first cycle and the last cycle are adopted for model verification. The terminal voltages and their errors are shown in Figure 21. In the model verification in Figure 21, the maximum solid-phase Li-ion concentration of positive and negative electrodes are identified by the CCPSO algorithm, while in the model verification in Figure 20, the reference values are adopted for above parameters.

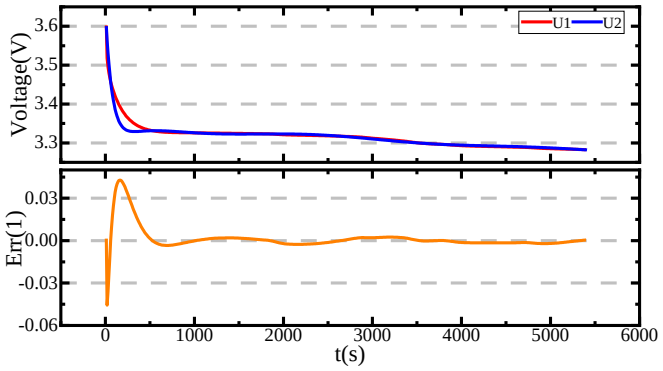

(A) Model verification of *Cell*2 during the first cycle

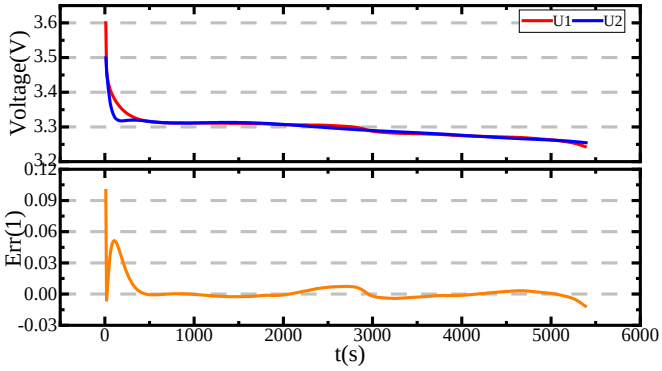

(B) Model verification of *Cell*2 during the last cycle

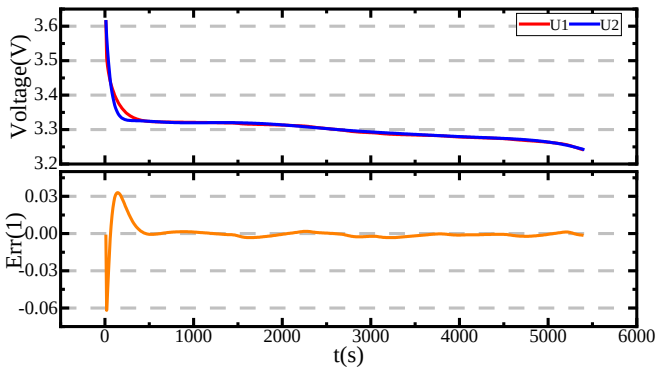

(C) Model verification of *Pack*1-1 during the first cycle

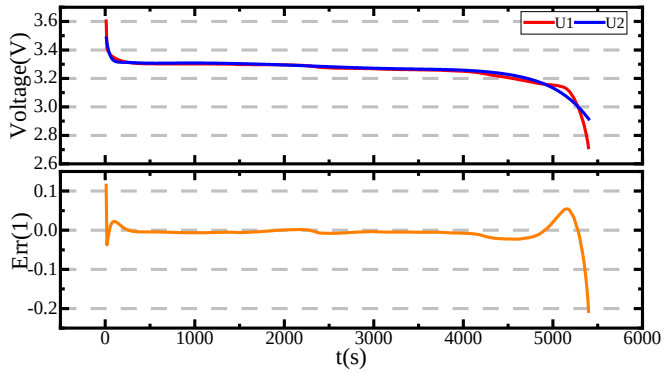

(D) Model verification of *Pack*1-1 during the last cycle

Figure 21 Model verification curves of *Cell*2 and *Pack*1-1

In Figure 21, *U*1 and *U*2 represent the actual and ESP model fitting terminal voltages. The comparison of (A), (B) or (C), (D) in Figure 21 shows that compared with the brand-new cell and battery pack, the voltage of the degraded cell and pack decreases significantly after the same time of discharge. It indicates that the capacity

performance is reduced after battery degradation. The MAEs of ESP model in *Cell*2 and *Pack*1-1 are shown in Table 6 .

Table 6 The MAEs of ESP model in *Cell*2 and *Pack*1-1

Cell	MAE of the first cycle	MAE of the last cycle
*Cell*2	0.00339 V	0.00431 V
*Pack*1-1	0.00257 V	0.0112 V

As can be analyzed from Figure 21 and Table 6, the errors of ESP model are very small under two low-rate cyclic conditions. In addition, in Table 6, by comparing the voltage MAEs during the first cycle and the last cycle, it can be known that under these conditions, with degradation, the accuracy of ESP model dips slightly within an acceptable range. In terms of model simulation accuracy, the above analysis results verify the effectiveness of the studied ESP model under low-rate cyclic conditions.

The cells under the variable-rate cyclic condition are modeled for verifying the proposed ESP model. In this research, *Pack*2 is in the variable-rate condition. During the first degradation cycle of *Pack*2-1, the curves of actual and fitting terminal voltages are shown in Figure 22.

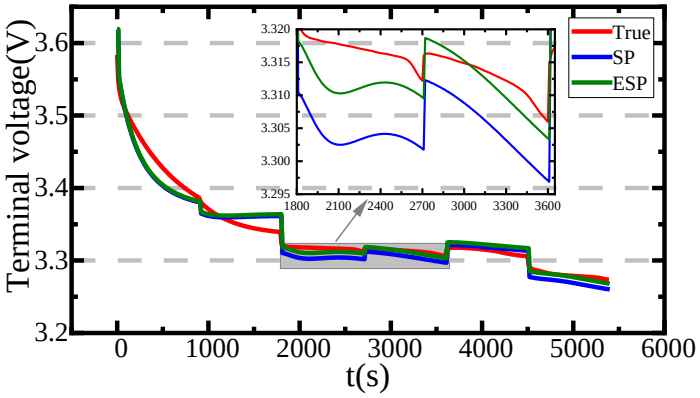

Figure 22 The actual and fitting terminal voltages of *Pack*2-1 during the first cycle

Specifically, in Figure 22, the MAEs of two fitting terminal voltages are elaborated in Table 7.

Table 7 The MAEs of model fitting terminal voltages

Cell and model	*Pack*2-1 in SP model	*Pack*2-1 in ESP model
MAE	0.01128 V	0.00838 V

Table 7 demonstrates that the fitting performance of ESP model is better under the variable-rate condition. In addition, *Pack*2-1 is adopted to verify the ESP model under this condition. The terminal voltages and

corresponding errors are demonstrated in Figure 23.

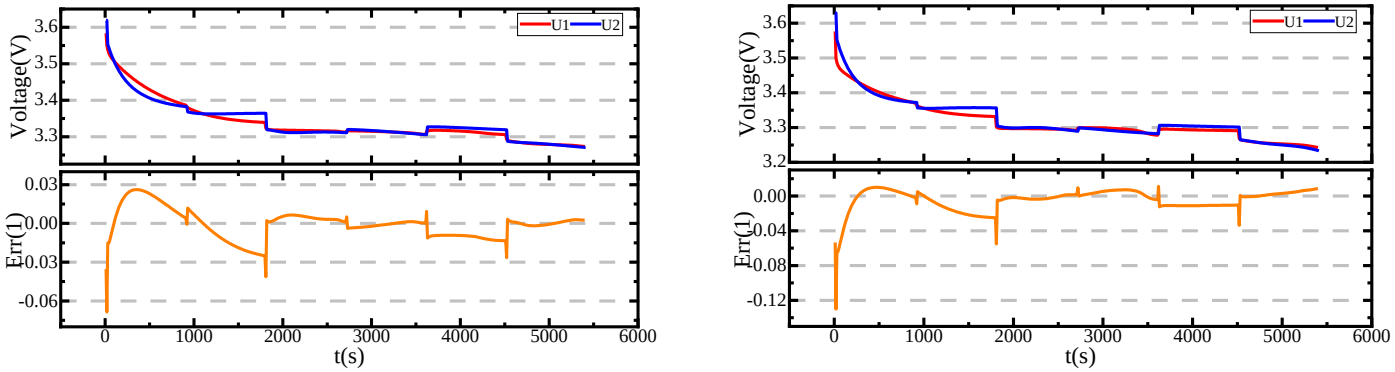

(A) Model verification of *Pack*2-1 during the first cycle

(B) Model verification of *Pack*2-1 during the last cycle

Figure 23 Model verification curves of *Pack*2-1

In Figure 23, *U*1 and *U*2 represent the actual and ESP model fitting terminal voltages. The comparison of (A) and (B) in Figure 23 indicates that the capacity performance is reduced after battery degradation. The MAEs of ESP model in *Pack*2-1 are shown in Table 8.

Table 8 The MAEs of ESP model in *Pack*2-1

Cell	MAE of the first cycle	MAE of the last cycle
*Pack*2-1	0.00822 V	0.00847 V

Through the analysis of Table 6 and Table 8, it can be observed that although the fitting effect of terminal voltage under the variable-rate condition is not as good as that under low-rate conditions, the corresponding fitting errors are still small. Besides, in Table 8, by comparing the voltage MAEs during the first cycle and the last cycle, it can be known that under this condition, with degradation, the accuracy of ESP model dips slightly within an acceptable range as well. In terms of model simulation accuracy, the above analysis results verify the effectiveness of the proposed ESP model under the self-designed variable-rate cyclic condition.

Table 6 and Table 8 show that during degradation, the decrease in ESP model accuracy reflects an increase in the identification errors of $c_{s,max,p}$ and $c_{s,max,n}$. Due to the above-mentioned electrochemical parameters are regarded as the input to the SOH estimation model, the increase in their errors have a negative impact on the estimation of SOH. In addition, Table 6 and Table 8 illustrate the accuracy of the ESP model, which confirms the effectiveness of the electrochemical parameter identification results based on the CCPSO algorithm in

Section 3.2.

3.4. Analysis of SOH estimation results under complex conditions

In this research, the SOH estimation results are analyzed under two low-rate conditions and one variable-rate condition. Firstly, under the low-rate conditions, $c_{s,max,p}$, $c_{s,max,n}$, LAM and LLI are taken as the input of neural network, and the SOH is taken as the output of neural network. Secondly, based on the four extracted HIs, the BP model, the simulated annealing-back propagation (SA-BP) model and the NSA-BP model are used to train and test the SOH estimation model. The settings of network structural parameters in above models are shown in Table 9.

Table 9 The settings of network structural parameters

Parameter	Notation	Value (unit) /Type
Initial temperature	T_0	8 (℃)
Final temperature	T_f	3 (℃)
Temperature drop rate in SA method	λ	0.85 (/)
Iteration cycles in NSA method	K_{max}	42 (/)
Step factor	c	0.2 (/)
Markov length	L	10 (/)
Node number of input layer	/	2 (/)
Node number of hidden layer	/	5 (/)
Node number of output layer	/	1 (/)
Learning rate/ rule	/	0.01 (/)/ L-M
termination target of training	/	1×10^{-3} (/)/ mean squared error
Activation function in hidden layer	/	Sigmoid
Activation function in output layer	/	Purelin

The relevant data of *Cell*2 is used as the training set, and in the low-rate cyclic conditions, the relevant data of *Pack*1 are used as the test set. For this test set, the SOH curves and the corresponding error curves are shown in Figure 24.

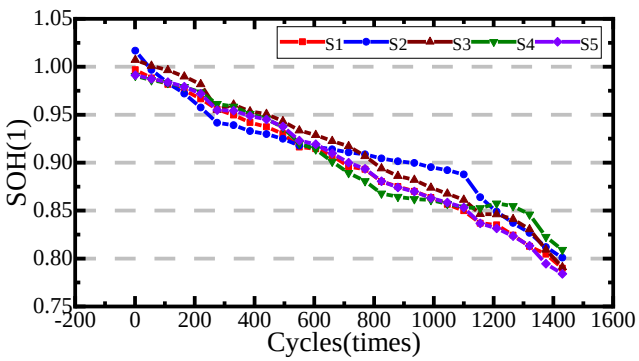

(A) Estimated and actual SOH values of *Pack*1-1

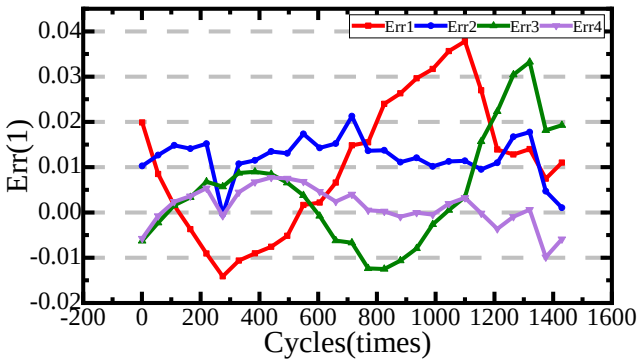

(B) Estimated and actual SOH errors of *Pack*1-1

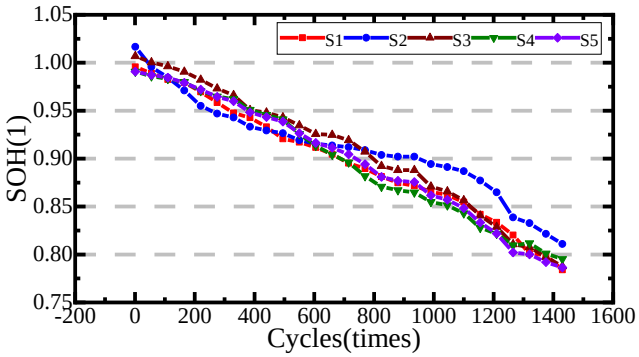

(C) Estimated and actual SOH values of *Pack*1-2

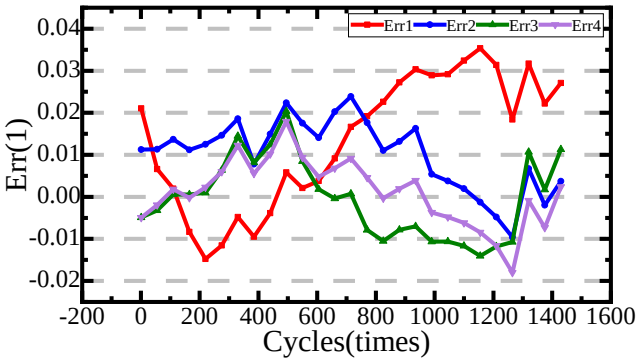

(D) Estimated and actual SOH errors of *Pack*1-2

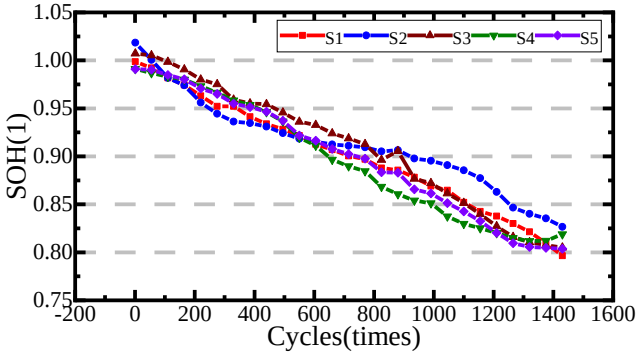

(E) Estimated and actual SOH values of *Pack*1-3

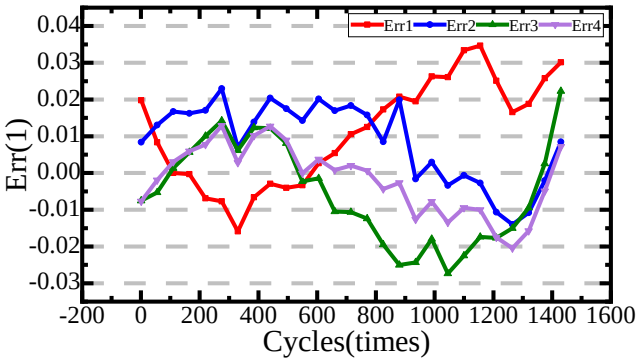

(F) Estimated and actual SOH errors of *Pack*1-3

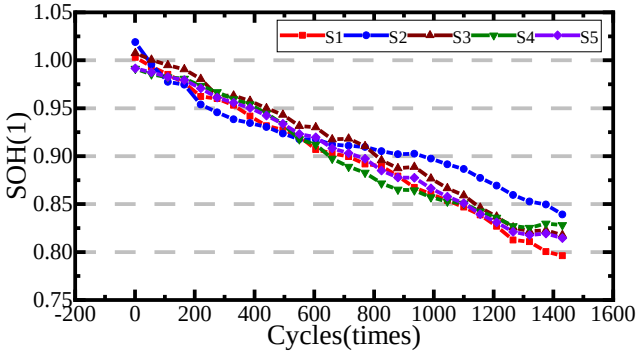

(G) Estimated and actual SOH values of *Pack*1-4

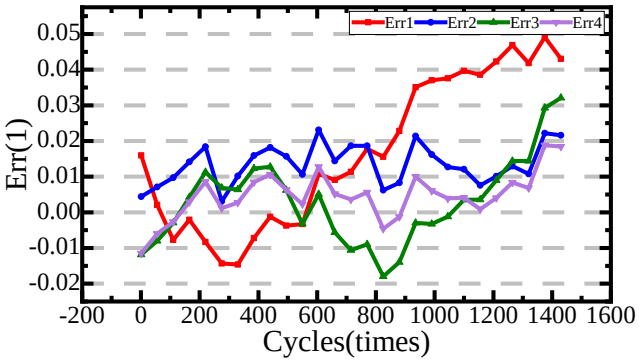

(H) Estimated and actual SOH errors of *Pack*1-4

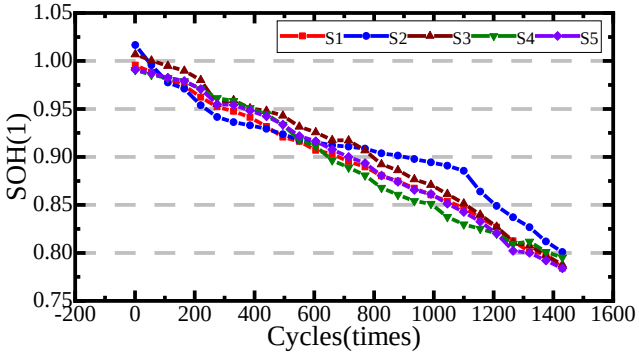

(I) Estimated and actual SOH values of *Pack*1

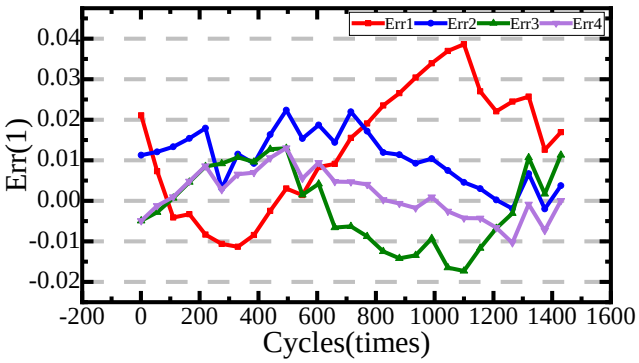

(J) Estimated and actual SOH errors of *Pack*1

Figure 24 The SOH values and corresponding errors of *Pack*1 and its cells

In Figure 24, *S*1, *S*2, *S*3, *S*4 and *S*5 denote the actual SOH, the SOH estimated on BP and $c_{s,max,i}$, the SOH estimated on BP and all proposed HIs, the SOH estimated on SA-BP and all proposed HIs, and the SOH estimated on NSA-BP and all proposed HIs, respectively. *Err*1, *Err*2, *Err*3 and *Err*4 denote the SOH errors of *S*2, the SOH errors of *S*3, the SOH errors of *S*4, and the SOH errors of *S*5, respectively. The evaluation indicators of above-mentioned approaches in *Pack*1 are shown in Table 10.

Table 10 Evaluation indicators of above-mentioned approaches in *Pack*1

Approach	*Pack*1-1	*Pack*1-2	*Pack*1-3	*Pack*1-4	*Pack*1
*S*2	RMSE: 0.01812 MAE: 0.01489	RMSE: 0.02065 MAE: 0.01763	RMSE: 0.01807 MAE: 0.01481	RMSE: 0.02679 MAE: 0.02152	RMSE: 0.01991 MAE: 0.01671
*S*3	RMSE: 0.01297 MAE: 0.01221	RMSE: 0.01312 MAE: 0.01151	RMSE: 0.01370 MAE: 0.01203	RMSE: 0.01464 MAE: 0.01353	RMSE: 0.01254 MAE: 0.01078
*S*4	RMSE: 0.01287 MAE: 0.00976	RMSE: 0.00927 MAE: 0.00778	RMSE: 0.01473 MAE: 0.01261	RMSE: 0.01217 MAE: 0.00970	RMSE: 0.00969 MAE: 0.00861
*S*5	RMSE: 0.00442 MAE: 0.00339	RMSE: 0.00764 MAE: 0.00622	RMSE: 0.00935 MAE: 0.00767	RMSE: 0.00802 MAE: 0.00659	RMSE: 0.00588 MAE: 0.00481

In Table 10, *S*2, *S*3, *S*4 and *S*5 have the same meaning as in Figure 24. As can be seen from Table 10, for *Pack*1 and each cell in *Pack*1, the SOH estimation approach based on all proposed HIs and NSA-BP model is significantly better in terms of RMSE and MAE indicators.

Because the developed quantification method can only be employed under low-rate conditions, under the self-designed variable-rate condition, only $c_{s,max,p}$ and $c_{s,max,n}$ are regarded as the input to train and test the SOH estimation model. In this case, the settings of network structural parameters are the same as those in Table 9. In the variable-rate cyclic condition, the relevant data of *Pack*2 are used as the test set. For this test set, the SOH curves and the corresponding error curves are shown in Figure 25.

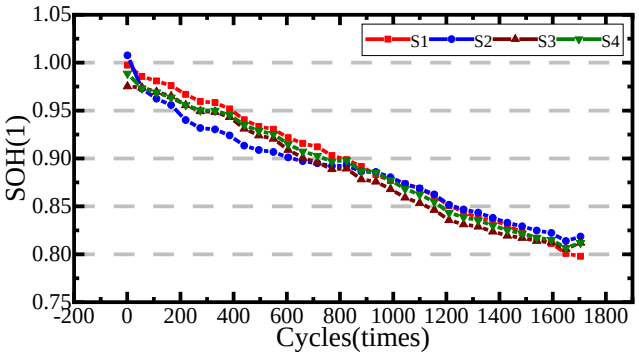

(A) Estimated and actual SOH values of *Pack*2-1

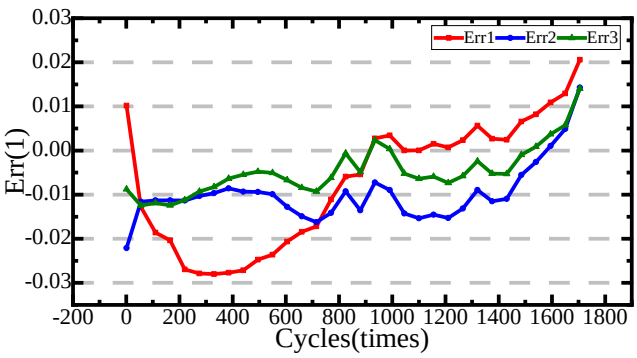

(B) Estimated and actual SOH errors of *Pack*2-1

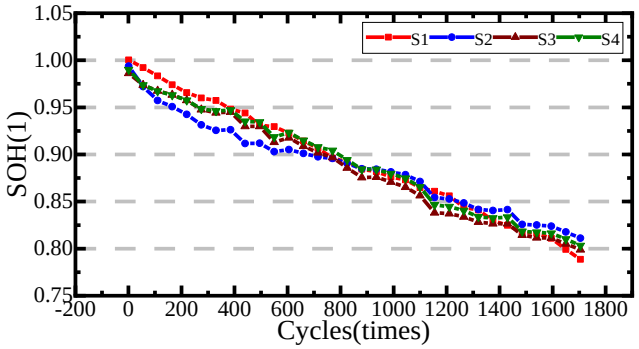

(C) Estimated and actual SOH values of *Pack*2-2

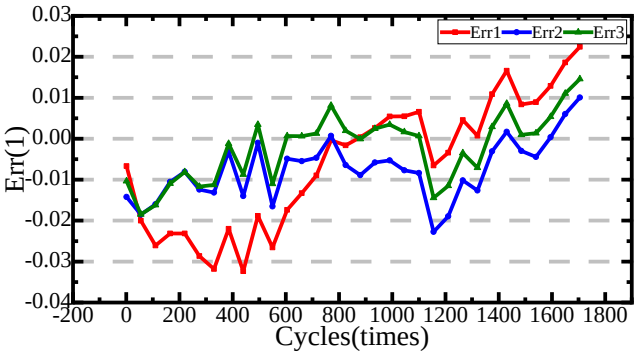

(D) Estimated and actual SOH errors of *Pack*2-2

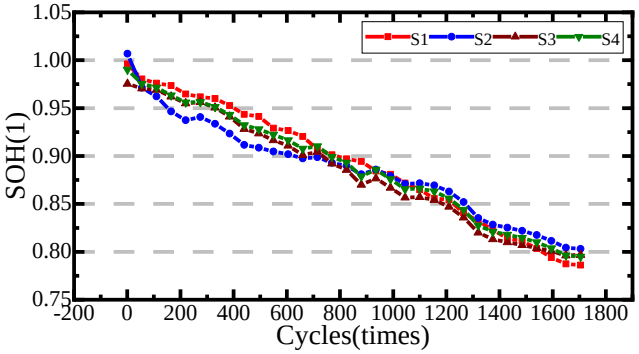

(E) Estimated and actual SOH values of *Pack*2-3

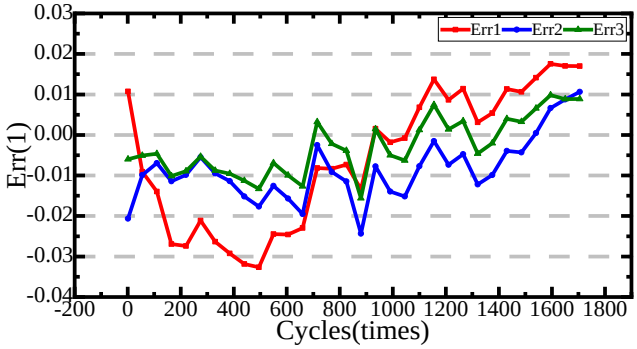

(F) Estimated and actual SOH errors of *Pack*2-3

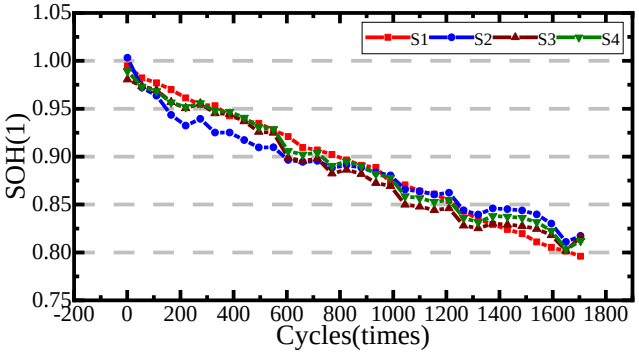

(G) Estimated and actual SOH values of *Pack*2-4

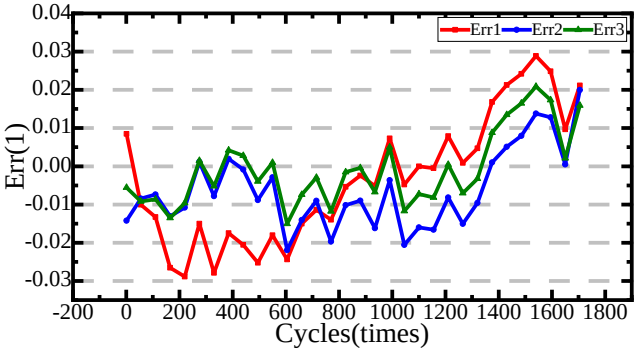

(H) Estimated and actual SOH errors of *Pack*2-4

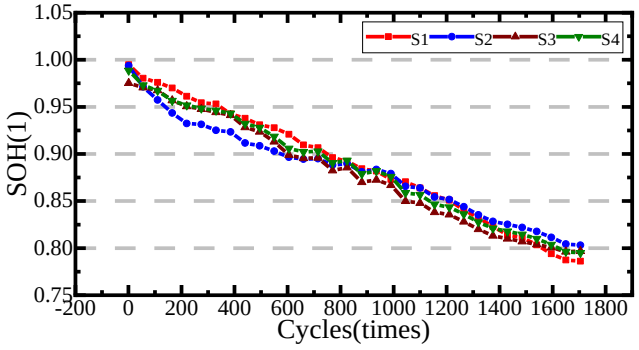

(I) Estimated and actual SOH values of *Pack*2

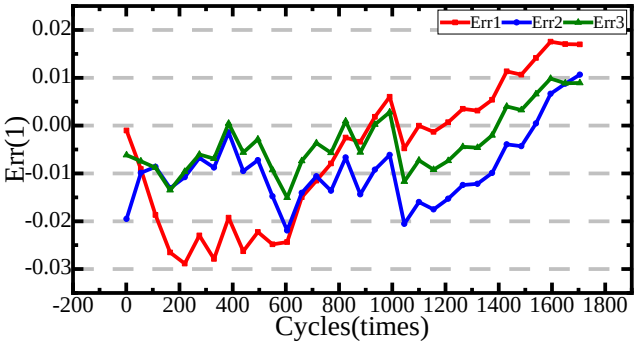

(J) Estimated and actual SOH errors of *Pack*2

Figure 25 The SOH values and corresponding errors of *Pack*2 and its cells

In Figure 25, *S*1, *S*2, *S*3 and *S*4 stand for the actual SOH, the SOH estimated on BP and $c_{s,max,i}$, the SOH estimated on SA-BP and $c_{s,max,i}$, and the SOH estimated on NSA-BP and $c_{s,max,i}$, respectively. In addition, *Err*1, *Err*2, and *Err*3 denote the SOH errors of *S*2, the SOH errors of *S*3, and the SOH errors of *S*4, respectively. From Figure 25, it can be intuitively observed that as degradation, in *Pack*2, the estimation accuracy of SOH for all cells and the pack shows a decreasing trend. This trend is particularly evident in the later stages of degradation. The evaluation indicators of above-mentioned approaches in *Pack*2 are shown in Table 11.

Table 11 Evaluation indicators of above-mentioned approaches in *Pack*2

Approach	*Pack*2-1	*Pack*2-2	*Pack*2-3	*Pack*2-4	*Pack*2
*S*2	RMSE: 0.01591 MAE: 0.01268	RMSE: 0.01671 MAE: 0.01362	RMSE: 0.01764 MAE: 0.01501	RMSE: 0.01703 MAE: 0.01440	RMSE: 0.01566 MAE: 0.01269
*S*3	RMSE: 0.01177 MAE: 0.01109	RMSE: 0.01037 MAE: 0.00866	RMSE: 0.01156 MAE: 0.01033	RMSE: 0.01191 MAE: 0.01030	RMSE: 0.01188 MAE: 0.01084
*S*4	RMSE: 0.00728 MAE: 0.00642	RMSE: 0.00845 MAE: 0.00673	RMSE: 0.00761 MAE: 0.00659	RMSE: 0.00953 MAE: 0.00776	RMSE: 0.00732 MAE: 0.00639

In Table 11, *S*2, *S*3 and *S*4 have the same meaning as in Figure 25. As can be seen from Table 11, for *Pack*2 and each cell in *Pack*2, the SOH estimation approach based on $c_{s,max,i}$ and NSA-BP model is also significantly better in terms of RMSE and MAE indicators. Combined with Table 10 and Table 11, the proposed algorithm can effectively and accurately estimate the long-term SOH of energy storage batteries of the fixed model under different working conditions. Besides, to prove the superiority of the developed method, it is compared with several recent advanced SOH estimation methods, as shown in Table 12. The comparison aspects cover RMSE, MAE, multi-condition estimation and pack estimation. Among them, the methods used for comparison are IC, DV, SVM, LSTM, deep convolutional neural network (DCNN), deep transfer convolutional neural network (DTCNN) and GRUNN. Under the experimental variable-rate cyclic condition, the aforementioned diverse methods are reproduced to compare their estimation performance with the proposed method. The comparison of various SOH estimation methods is demonstrated in Table 12.

Table 12 The comparison of various SOH estimation methods

SOH estimation methods	Refs.	RMSE	MAE	Multi-condition estimation	Pack estimation
IC-based	[58]	2.371%	3.039%	Not mentioned	Not mentioned
DV-based	[56]	1.968%	2.834%	Not mentioned	Available in series pack
SVM-based	[40]	1.542%	1.491%	Not mentioned	Not mentioned
LSTM-based	[59]	0.977%	0.713%	Not mentioned	Not mentioned
DCNN-based	[60]	1.306%	1.124%	Not mentioned	Not mentioned

DTCNN-based	[61]	0.521%	0.663%	Not mentioned	Not mentioned
GRUNN-based	[48]	0.737%	0.590%	Not mentioned	Not mentioned
Proposed method	-	0.728%	0.642%	Available in various condition	Available in series pack

Most advanced methods used for comparison are currently only applicable to individual cells, so the RMSE and MAE in Table 12 are calculated based on experimental data from *Pack*2-1. From Table 12, it is evident that, in terms of above-mentioned four aspects, the method proposed in this research outperforms other recent advanced methods in most cases. Although the developed method is inferior to the DTCNN-based method in RMSE and GRUNN-based method in MAE, the corresponding gaps are small, and the method raised in this study has the advantages of multi-condition estimation ability and pack state estimation ability. Data from laboratory tests throughout the degradation cycle is conveniently accessible at the following URLs: https://www.researchgate.net/publication/376028814_energy_storage_experimental_data.

4. Conclusions

The efficient estimation of battery SOH is important and urgent for the new energy storage system. Based on this requirement, this research constructs a SOH estimation method based on CCPSO algorithm and NSA-BP method. Firstly, the improvement effect and the contribution of CCPSO algorithm are highlighted. Secondly, multi-dimensional HIs are extracted by CCPSO algorithm, ESP model and IC-DV curves. Lastly, the above HIs are used to train and test the NSA-BP model to estimate the SOH degradation sequences. In the designed energy storage experiments, it shows that in most cases, the RMSE and the MAE of the developed SOH estimation method are better compared with algorithms before improvement and some advanced methods. The limitations of this work include the inability to meet high real-time estimation, the failure to consider the actual complex energy storage system structure, and the failure to consider more actual energy storage conditions and batteries. Future work can focus on the following parts:

1) Research on SOH estimation of series-parallel battery systems and the internal coupling mechanism.

2) Research on SOH estimation to meet higher real-time requirements.

3) Research on SOH estimation under more energy storage conditions and more types of batteries.

Acknowledgments

The authors acknowledge the financial support from National Natural Science Foundation of China (No. 61801407), China Scholarship Council (No.201908515099), and Fund of Robot Technology Used for Special Environment Key Laboratory of Sichuan Province (No.18kftk03).

References

[1] Cho J, Jeong S, Kim Y. Commercial and research battery technologies for electrical energy storage applications. Progress in Energy and Combustion Science. 2015;48:84-101.

[2] Liu L, Yan Z, Xu B, Zhang P, Cai C, Yang H. A Highly Scalable Integrated Voltage Equalizer Based on Parallel-Transformers for High-Voltage Energy Storage Systems. IEEE Transactions on Industrial Electronics. 2023;1:1-8.

[3] Abbott M, Cohen B. Issues associated with the possible contribution of battery energy storage in ensuring a stable electricity system. The Electricity Journal. 2020;33:106771-106781.

[4] Zhang C, Zhao S, He Y. An Integrated Method of the Future Capacity and RUL Prediction for Lithium-Ion Battery Pack. IEEE Transactions on Vehicular Technology. 2022;71:2601-2613.

[5] Ren H, Zhao Y, Chen S, Wang T. Design and implementation of a battery management system with active charge balance based on the SOC and SOH online estimation. Energy. 2019;166:908-917.

[6] Liu X, Li J, Yao Z, Wang Z, Si R, Diao Y. Research on battery SOH estimation algorithm of energy storage frequency modulation system. Energy Reports. 2022;8:217-223.

[7] Feng F, Hu X, Hu L, Hu F, Li Y, Zhang L. Propagation mechanisms and diagnosis of parameter inconsistency within Li-Ion battery packs. Renewable and Sustainable Energy Reviews. 2019;112:1-18.

[8] Chaoui H, Ibe-Ekeocha CC, Gualous H. Aging prediction and state of charge estimation of a LiFePO4 battery using input time-delayed neural networks. Electric Power Systems Research. 2017;146:189-197.

[9] Zhou X, L.Stein J, Ersal T. Battery state of health monitoring by estimation of the number of cyclable Li-ions. Control Engineering Practice. 2017;66:51-63.

[10] Prasad GK, Rahn CD. Model based identification of aging parameters in lithium ion batteries. Journal of Power Sources. 2013;232:79-85.

[11] Diao W, Jiang J, Zhang C, Liang H, Pecht M. Energy state of health estimation for battery packs based on the degradation and inconsistency. Energy Procedia. 2017;142:3578-3583.

[12] Xu L, Deng Z, Hu X. Battery health estimation using electrochemical aging model and ensemble kalman filtering. IEEE International Future Energy Electronics Conference. 2021;1:1-6.

[13] Park J, Lee M, Kim G, Park S, Kim J. Integrated approach based on dual extended Kalman filter and multivariate autoregressive model for predicting battery capacity using health indicator and SOC/SOH. Energies. 2020;13:2138-2150.

[14] Xiong R, Wang S, Yu C, Fernandez C, Xiao W, Jia J. A novel nonlinear decreasing step-bacterial foraging optimization algorithm and simulated annealing-back propagation model for long-term battery state of health estimation. Journal of Energy Storage. 2023;59:106484-106495.

[15] Tian H, Qin P, Li K, Zhao Z. A review of the state of health for lithium-ion batteries: Research status and suggestions. Journal of Cleaner Production. 2020;261:120813-120821.

[16] Akash B, Zineb S-A, Eric G, Peggy Z. Review on state of health estimation methodologies for lithium-ion batteries in the context of circular economy. CIRP Journal of Manufacturing Science and Technology. 2021;32:517-528.

[17] Tian J, Xiong R, Shen W, Lu J, Sun F. Flexible battery state of health and state of charge estimation using partial charging data and deep learning. Energy Storage Materials. 2022;51:372-381.

[18] Tian J, Xiong R, Shen W. State-of-health estimation based on differential temperature for lithium ion batteries. IEEE

Transactions on Power Electronics. 2020;35:10363-10373.
[19] Jiang S, Song Z. A review on the state of health estimation methods of lead-acid batteries. Journal of Power Sources. 2022;517:230710-230721.
[20] Wen J, Zou Q, Chen C, Wei Y. Linear correlation between state-of-health and incremental state-of-charge in Li-ion batteries and its application to SoH evaluation. Electrochimica Acta. 2022;434:141300-141311.
[21] Lee J, Won J. Enhanced Coulomb Counting Method for SoC and SoH Estimation Based on Coulombic Efficiency. IEEE Access. 2023;1:1-10.
[22] Bin X, Bing X, Luoshi L. Rapid measurement method for lithium- ion battery state of health estimation based on least squares support vector regression. International Journal of Energy Research. 2020;45:5695-5709.
[23] Wang S, Xiong X, Zou C, Chen L, Jiang C, Xie Y, et al. An improved coulomb counting method based on dual open- circuit voltage and real- time evaluation of battery dischargeable capacity considering temperature and battery aging. International Journal of Energy Research. 2021;45:17609-17621.
[24] Chen M, Ma G, Liu W, Zeng N, Luo X. An Overview of Data-driven Battery Health Estimation Technology for Battery Management System. Neurocomputing. 2023;1:1-9.
[25] Messing M, Shoa T, Habibi S. Estimating battery state of health using electrochemical impedance spectroscopy and the relaxation effect. Journal of Energy Storage. 2021;43:103210-103221.
[26] Hu X, Li S, Peng H. A comparative study of equivalent circuit models for Li-ion batteries. Journal of Power Sources. 2011;198:359-367.
[27] Qiao J, Wang S, Yu C, Yang X, Fernandez C. A chaotic firefly - Particle filtering method of dynamic migration modeling for the state-of-charge and state-of-health co-estimation of a lithium-ion battery performance. Energy. 2023;263:126164-126174.
[28] Wu T, Liu S, Wang Z, Huang Y. SOC and SOH Joint Estimation of Lithium-Ion Battery Based on Improved Particle Filter Algorithm. Journal of Electrical Engineering & Technology. 2022;17:307–317.
[29] Lee JL, Chemistruck A, Plett GL. One-dimensional physics-based reduced-order model of lithium-ion dynamics. Journal of Power Sources. 2012;220:430-448.
[30] Lee JL, Aldrich LL, Stetzel KD, Plett GL. Extended operating range for reduced-order model of lithium-ion cells. Journal of Power Sources. 2014;255:85-100.
[31] Li J, Adewuyi K, Lotfi N, Landers RG, Park J. A single particle model with chemical/mechanical degradation physics for lithium ion battery State of Health (SOH) estimation. Applied Energy. 2018;212:1178-1190.
[32] Wu S, Pan W, Zhu M. A Collaborative Estimation Scheme for Lithium-Ion Battery State of Charge and State of Health Based on Electrochemical Model. Journal of The Electrochemical Society. 2022;169:1-14.
[33] Lipu MSH, Hannan MA, Hussain A, Hoque MM, Ker PJ, Saad MHM, et al. A review of state of health and remaining useful life estimation methods for lithium-ion battery in electric vehicles: Challenges and recommendations. Journal of Cleaner Production. 2018;205:115-133.
[34] Ge M, Liu Y, Jiang X, Liu J. A review on state of health estimations and remaining useful life prognostics of lithium-ion batteries. Measurement. 2021;174:109057-109064.
[35] Xin S, Shan H, B. VS, Jinhao M, Remus T, Daniel-Ioan S. A review of non-probabilistic machine learning-based state of health estimation techniques for Lithium-ion battery. Applied Energy. 2021;300:117346-117357.
[36] Zhao S, Zhang C, Wang Y. Lithium-ion Battery Capacity and Remaining Useful Life Prediction Using Board Learning System and Long Short-Term Memory Neural Network. Journal of Energy Storage. 2022;52:104901-104909.
[37] Li P, Zhang Z, Xiong Q, Ding B, Hou J, Luo D, et al. State-of-health estimation and remaining useful life prediction for the lithium-ion battery based on a variant long short term memory neural network. Journal of Power Sources. 2020;459:228069-228078.
[38] Bockrath S, Lorentz V, Pruckner M. State of health estimation of lithium-ion batteries with a temporal convolutional neural network using partial load profiles. Applied Energy. 2023;329:120307-120318.
[39] Gu X, See KW, Li P, Shan K, Wang Y, Zhao L, et al. A novel state-of-health estimation for the lithium-ion battery

using a convolutional neural network and transformer model. Energy. 2023;262:125501-125514.
[40] Liu Z, Zhao J, Wang H, Yang C. A New Lithium-Ion Battery SOH Estimation Method Based on an Indirect Enhanced Health Indicator and Support Vector Regression in PHMs. Energies. 2020;13:1-14.
[41] He J, Bian X, Liu L, Wei Z, Yan F. Comparative study of curve determination methods for incremental capacity analysis and state of health estimation of lithium-ion battery. Journal of Energy Storage. 2020;29:101400-101409.
[42] Seho S, Siheon J, Eunji K, Jun-hyeong K, Ki-Yong O. Integrated framework for SOH estimation of lithium-ion batteries using multiphysics features. Energy. 2022;238:121712-121721.
[43] Xu X, Tang S, Ren H, Han X, Wu Y, Lu L, et al. Joint state estimation of lithium-ion batteries combining improved equivalent circuit model with electrochemical mechanism and diffusion process. Journal of Energy Storage. 2022;56:106135-106144.
[44] Liu G, Zhang X, Liu Z. State of health estimation of power batteries based on multi-feature fusion models using stacking algorithm. Energy. 2022;259:124851-124865.
[45] Duan W, Song S, Xiao F, Chen Y, Peng S, Song C. Battery SOH estimation and RUL prediction framework based on variable forgetting factor online sequential extreme learning machine and particle filter. Journal of Energy Storage. 2023;65:107322-107341.
[46] Jiang Y, Chen Y, Yang F, Peng W. State of health estimation of lithium-ion battery with automatic feature extraction and self-attention learning mechanism. Journal of Power Sources. 2023;556:232466-232478.
[47] Deng Z, Lin X, Cai J, Hu X. Battery health estimation with degradation pattern recognition and transfer learning. Journal of Power Sources. 2022;525:231027-231038.
[48] Chen Z, Zhao H, Zhang Y, Shen S, Shen J, Liu Y. State of health estimation for lithium-ion batteries based on temperature prediction and gated recurrent unit neural network. Journal of Power Sources. 2022;521:230892-230904.
[49] Luo W, Lyu C, Wang L, Zhang L. An approximate solution for electrolyte concentration distribution in physics-based lithium-ion cell models. Microelectronics Reliability. 2013;53:797-804.
[50] Li X, Ju L, Geng G, Jiang Q. Data-driven state-of-health estimation for lithium-ion battery based on aging features. Energy. 2023;274:127378-127388.
[51] Wu Z, Yin L, Xiong R, Wang S, Xiao W, Liu Y, et al. A novel state of health estimation of lithium-ion battery energy storage system based on linear decreasing weight-particle swarm optimization algorithm and incremental capacity-differential voltage method. International Journal of Electrochemical Science. 2022;17:1-32.
[52] Pastor-Fernández C, Uddin K, Chouchelamane GH, Widanage WD, Marco J. A Comparison between Electrochemical Impedance Spectroscopy and Incremental Capacity-Differential Voltage as Li-ion Diagnostic Techniques to Identify and Quantify the Effects of Degradation Modes within Battery Management Systems. Journal of Power Sources. 2017;360:301-308.
[53] Anseán D, Manuel V, Manuela G, Cecilio G, Blanco-Viejo. Lithium-Ion Battery Degradation Indicators Via Incremental Capacity Analysis. IEEE Transactions on Industry Applications. 2019;55:1-10.
[54] Lewerenz M, Marongiu A, Warnecke A, Sauer DU. Differential voltage analysis as a tool for analyzing inhomogeneous aging: A case study for LiFePO4 |Graphite cylindrical cells. Journal of Power Sources. 2017;368:57-67.
[55] Cordoba-Arenas A, Onori S, Rizzoni G. A control-oriented lithium-ion battery pack model for plug-in hybrid electric vehicle cycle-life studies and system design with consideration of health management. Journal of Power Sources. 2015;279:1-13.
[56] Berecibar M, Garmendia M, Gandiaga I, Crego J, Villarreal I. State of health estimation algorithm of LiFePO4 battery packs based on differential voltage curves for battery management system application. Energy. 2016;103:784-796.
[57] Safari M, Delacourt C. Modeling of a Commercial Graphite/LiFePO4 Cell. Journal of The Electrochemical Society. 2011;158:562-571.
[58] Li X, Wang Z, Zhang L, Zou C, Dorrell DD. State-of-health estimation for Li-ion batteries by combing the incremental capacity analysis method with grey relational analysis. Journal of Power Sources. 2019;410-411:106-114.
[59] Li K, Wang Y, Chen Z. A comparative study of battery state-of-health estimation based on empirical mode

decomposition and neural network. Journal of Energy Storage. 2022;54:105333-105348.
[60] Shen S, Sadoughi M, Chen X, Hong M, Hu C. A deep learning method for online capacity estimation of lithium-ion batteries. Journal of Energy Storage. 2019;25:100817-100825.
[61] Yao J, Han T. Data-driven lithium-ion batteries capacity estimation based on deep transfer learning using partial segment of charging/discharging data. Energy. 2023;24:127033-127042.